Electronic Supplementary Material (ESI) for ChemComm.

Table of Contents

I. General

Solvents and commercial starting materials were purchased from Sigma Aldrich, TCI, Fisher Scientific, J&K scientific, fluorochem and abcr GmbH and used as received. Dry solvents were obtained from an MBraun solvent purification system. Reactions were monitored by thin layer chromatography (TLC) carried out on silica gel plates (ALUGRAM® Xtra SIL G/UV254, Macherey Nagel) using UV light for detection. Column chromatography was carried out with silica gel (Silica 60 M, 0.04-0.063 mm, Macherey Nagel) using eluents as specified. Flash column chromatography was carried out on a Biotage® Selekt system using the SNAP Sphär60 columns.

NMR measurements

NMR spectra were recorded on a Bruker Avance III 300 and a Bruker Avance III 600 spectrometer at 25 °C using residual protonated solvent signals as internal standards for ^{1}H spectra (^{1}H: $\delta(CDCl_3) = 7.26$ ppm). Splitting patterns are abbreviated as follows: singlet (s), doublet (d), triplet (t), quartet (q), quintet (p), heptet (hept), multiplet (m), and broad (br).

II. Experimental details

Synthesis of 1,2,4,5-tetrafluoro-3,6-diiodobenzene (I_2F_4)

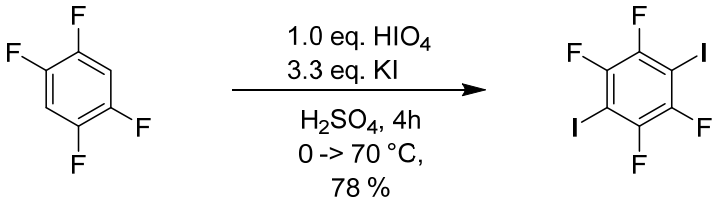

Potassium iodide (4.98 g, 30.0 mmol, 3.3 eq.) was added very slowly to a suspension of periodic acid (1.73 g, 9.00 mmol, 1.0 eq.) in concentrated H_2SO_4 (20 ml) at 0 °C. To the dark mixture, 1,2,4,5-tetrafluorobenzene (1.10 ml, 9.00 mmol, 1.0 eq.) was added dropwise. The suspension was heated to 70 °C for 4 h. The mixture was allowed to cool to room temperature and then poured onto ice. Aqueous solution was extracted with diethyl ether and the combined organic phases were washed with aqueous sodium thiosulfate solution and water. The solution was dried over magnesium sulfate and concentrated under reduced pressure. The crude product was purified by recrystallization from cyclohexane to give 1,2,4,5-tetrafluoro-3,6-diiodobenzene (**I_2F_4**) as colourless crystals (2.82 g, 7.00 mmol, 78 %).

$^{19}F\{^1H\}$-NMR (282 MHz, $CDCl_3$): δ = -118.1 (s, ArF) ppm.
Analytical data was in accordance with literature.[S1]

Synthesis of 1,3,5-trifluoro-2,4,6-triiodobenzene (I_3F_3)

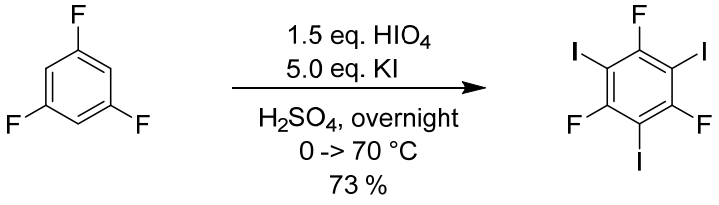

Potassium iodide (7.47 g, 45.0 mmol, 3.3 eq.) was added very slowly to a suspension of periodic acid (2.59 g, 9.00 mmol, 1.5 eq.) in concentrated H_2SO_4 (20 mL) at 0 °C. To the dark mixture, 1,2,4,5-tetrafluorobenzene (0.97 ml, 9.00 mmol, 1.0 eq.) was added dropwise. After finished addition, the

suspension was heated to 70 °C overnight. The mixture was allowed to cool to room temperature and then poured onto ice. The aqueous solution was extracted with diethyl ether and the combined organic phases were washed with aqueous sodium thiosulfate solution and water. The solution was dried over magnesium sulfate and concentrated under reduced pressure. The crude product was purified by recrystallization from cyclohexane to give 1,3,5-trifluoro-2,4,6-triiodobenzene (**I_3F_3**) as colourless needles (3.33 g, 6.53 mmol, 73 %).

$^{19}F\{^1H\}$-NMR (282 MHz, $CDCl_3$): δ = -68.9 (s, ArF) ppm.
Analytical data was in accordance with literature.[S2]

Synthesis of Imine Cages A and B

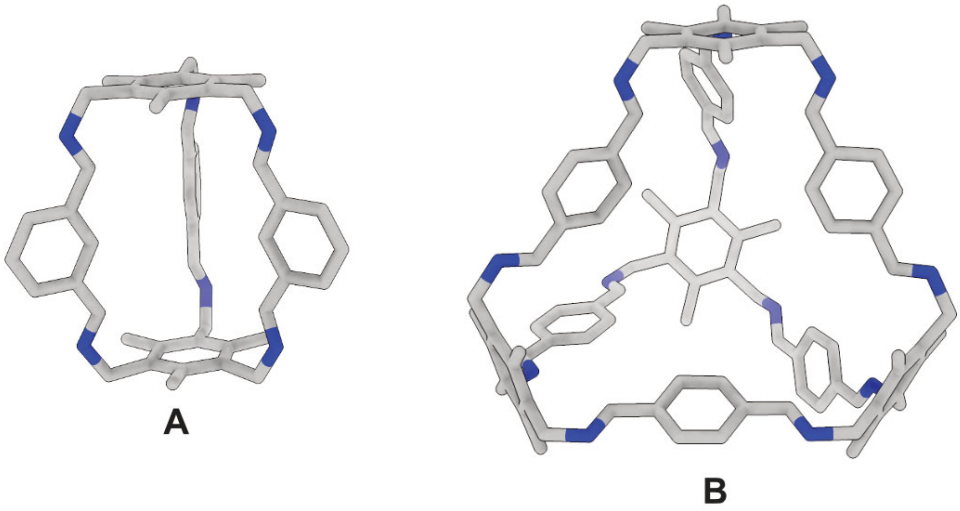

The cage compounds A and B were synthezied according to literature procedures.[S3]

Synthesis of A···IF_5

Slow evaporation of a solution of imine cage **A** (7.0 mg, 10 µmol, 1 eq.) and donor **IF_5** (1.3 µL, 10 µmol, 1.0 eq.) in a mixture of chloroform and methanol ($CHCl_3$:MeOH 10:1) led to the formation of crystalline **A···IF_5**.

Synthesis of A···2(I_2F_4)

Slow evaporation of a solution of imine cage **A** (7.0 mg, 10 µmol, 1 eq.) and donor **I_2F_4** (8.0 mg, 20 µmol, 2 eq.) in chloroform led to the formation of crystalline **A···2(I_2F_4)**.

Synthesis of A···4(I_3F_3)

Slow evaporation of a solution of imine cage **A** (7.0 mg, 10 μmol, 1 eq.) and donor **I_3F_3** (20 mg, 40 μmol, 4 eq.) in chloroform led to the formation of crystalline **A···4(I_3F_3)**.

Synthesis of B···2(I_2F_4)

Slow evaporation of a solution of imine cage **B** (7.0 mg, 5.0 μmol, 1 eq.) and donor **F_4I_2** (4.0 mg, 10 μmol, 2 eq.) in a mixture of chloroform and acetonitrile ($CHCl_3$:MeCN 10:1) led to the formation of crystalline **B···2(I_2F_4)**.

Halogen-bonded complex synthesis by liquid assisted grinding

Samples prepared liquid assisted grinding were obtained by using a MM 400 Retsch ball-mill. The starting materials were mixed in targeted stoichiometry with a small amount of the corresponding solvent and then grinded using 5 mm zirconium dioxide balls at 25 Hz for 15 minutes.

III. Association experiments

The constant component is referred to as “host” while the varied compound is called “guest”. 1,2,3,4,5-Pentafluoro-6-iodobenzene was used as the host and *N*-benzylideneaniline was chosen as guests. ^{19}F NMR spectra were recorded on a 300 MHz Bruker Avance III at 298 K. Hexafluorobenzene in C_6D_6 was added as an internal standard.

NMR Binding Experiments

The stock solution of the host (c = 11.51 mM) in cyclohexane was created using gravimetric analyses. This solution was then used to prepare the stock solution of the guest (*c* = 1.261 M). The guest was successively added to the host, keeping the total concentration of the host constant while the total concentration of the guest was varied. The titrations were carried out twice.

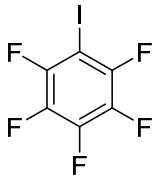

host

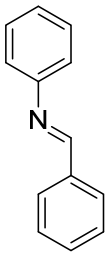

guest (G)

Table S1: Concentration of guest, equivalents of guest added in comparison to host and resulting shift in the ^{19}F NMR for both titrations.

$[G]_0$ in M	$[G]_0/[H]_0$	|Δδ(F)| in ppm	
		1	2
0.000	0.0	0.000	0.000
0.006	0.5	0.010	0.006
0.011	1.0	0.025	0.016
0.023	2.0	0.031	0.020
0.044	3.9	0.038	0.033
0.065	5.7	0.050	0.044
0.086	7.4	0.068	0.063
0.105	9.1	0.074	0.071
0.151	13.1	0.103	0.091
0.194	16.8	0.119	0.107
0.269	23.4	0.145	0.141
0.334	29.0	0.164	0.160
0.391	33.9	0.185	0.176
0.441	38.3	0.200	0.196
0.485	42.1	0.208	0.210

Using OriginPro 2018b, the graphs of the change of the chemical shift (Δδ) against the guest concentration $[G]_0$ were curve fitted using the orthogonal distance regression iteration algorithm. The following equation[S4] was used for curve fitting:

$$\Delta\delta = \frac{\Delta\delta_{sat}}{2}\left[\left(\frac{[G]_0}{[H]_0} + 1 + \frac{1}{K_a[H]_0}\right) - \sqrt{\left(\frac{[G]_0}{[H]_0} + 1 + \frac{1}{K_a[H]_0}\right)^2 - 4\frac{[G]_0}{[H]_0}}\right]$$

The total concentration of the host $[H]_0$ is constant while the total concentration of the guest $[G]_0$ is varied. The association constant K_a and the change in chemical shift for a saturated system are obtained by curve fitting.

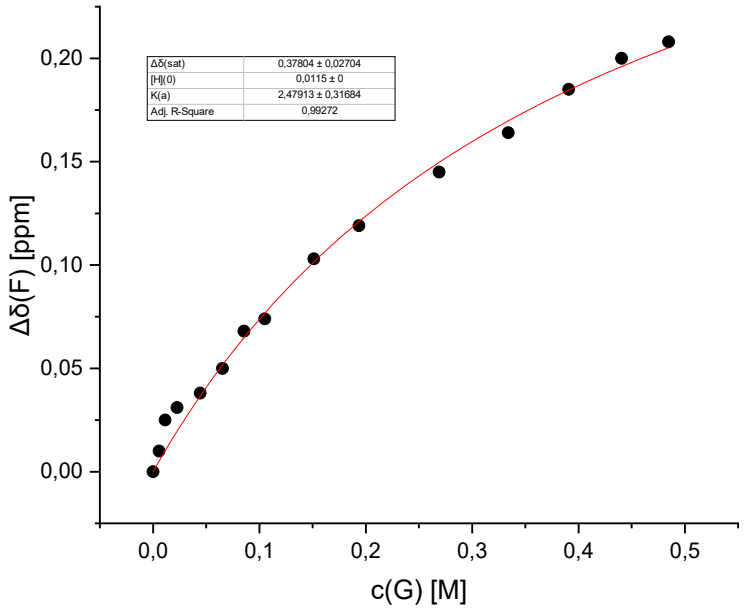

Figure S1: Binding titration 1.

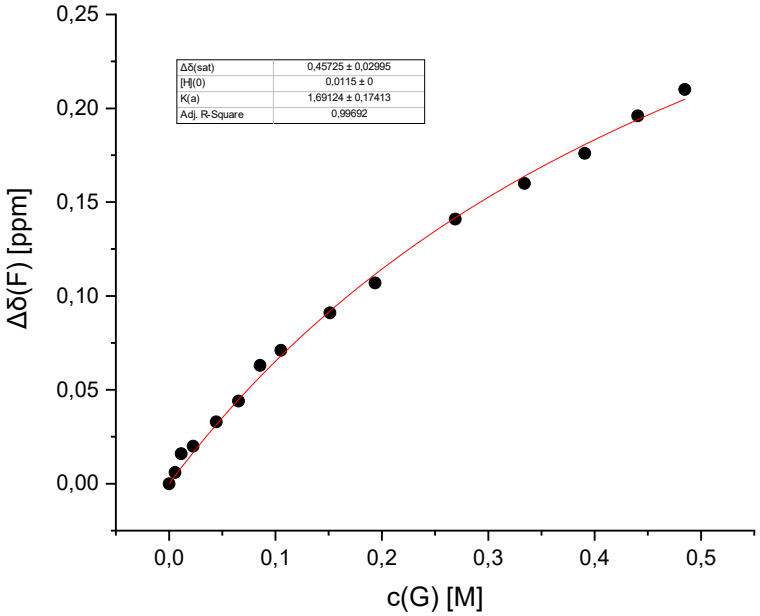

Figure S2: Binding titration 2.

The two determined binding constants for **G···IF$_5$** differ because of the very low association constant at room temperature. The shifts in the ^{19}F NMR spectra during the titration were very small, leading to the two values of K_a = 2.48 M^{-1} and K_a = 1.69 M^{-1}. Both values underline the weak binding of the model system in solution at room temperature and show the range of error.

IV. Crystallographic details

Single-crystals were mounted using a microfabricated polymer film crystal-mounting tool (dual-thickness MicroMount, MiTeGen) using low viscosity oil (perfluoropolyalkylether; viscosity 1800 cSt, ABCR). A Rigaku XtaLAB Synergy diffractometer or Bruker D8 QUEST single-crystal X-ray diffractometer using Mo-K_α (λ = 0.71073 Å) radiation were used for data collection at the temperature stated for each compound. The structures were refined by full-matrix least-squares methods on F^2 (SHELXL-2018).[S5] The hydrogen atoms were placed at calculated positions and refined by using a riding model. CCDC 2115251 (**A⋯IF$_5$**) CCDC 2115253 (**A⋯2(I$_2$F$_4$)**) CCDC 2115252 (**A⋯4(I$_3$F$_3$)**) and CCDC 2115254 (**B⋯2(I$_2$F$_4$)**) contain the supplementary crystallographic data for this paper. These data can be obtained free of charge from The Cambridge Crystallographic Data Centre.

A⋯IF$_5$

Crystals of **A⋯IF$_5$** were obtained by slow evaporation of a methanol/chloroform mixture at room temperature. A colourless block was mounted and data collection was performed at 153 K using Mo-K_α radiation. The structure was found to contain one well resolved methanol molecule enclosed into the centre of cage **A**. No other (disordered) solvent molecules were observed. However, the **IF$_5$** molecule displayed a minor rotational disorder (60°, 88:12 % occupancy) which was freely modelled and well resolved.

A⋯2(I$_2$F$_4$)

Crystals of **A⋯2(I$_2$F$_4$)** were grown by slow evaporation of a chloroform solution at room temperature. A colourless prism was mounted and data collection was performed at 100 K using Mo-K_α radiation. The cavities are filled with one partially disordered chloroform solvent molecule, which was modelled, and a second, heavily disordered chloroform molecule, that was ultimately removed using SQUEEZE.[S6] The solvent accessible volume (SAV) found was 370 Å^3 with 118 electrons (per unit cell). Platon[S7] suggested the presence of twinning and the structure was treated accordingly using the twinning routine.

A⋯4(I$_3$F$_3$)

Crystals of **A⋯4(I$_3$F$_3$)** were grown by slow evaporation of a saturated chloroform solution at room temperature. A colourless prism was mounted and data collection was performed at 100 K using Mo-K_α

radiation. The structure has three sites occupied by chloroform molecules each with three or more orientations. Modelling was attempted but all solvent molecules were ultimately removed using SQUEEZE.[S6] The solvent accessible volume (SAV) found was 1341 Å^3 with 392 electrons (per unit cell). Checkcif produces one B-Alert for this structure: "PLAT910_ALERT_3_B Missing # of FCF Reflection(s) Below Theta(Min). 11 Note" this is likely due to the beam-stop, originating from using Mo radiation in combination with the geometry of our goniometer.

B···2(I_2F_4)

Crystals of **B···2(I_2F_4)** were grown by slow evaporation of an acetonitrile/chloroform mixture at room temperature. A colourless plate was mounted and data collection was performed at 153 K using Mo-K_α radiation. The structure contained various sites of heavily disordered chloroform and acetonitrile molecules showing both, orientation and rotation disorder. Modelling was attempted but all solvent molecules were ultimately removed using SQUEEZE.[S6] The solvent accessible volume (SAV) found was 5109.9 Å^3 with 1658.5 electrons (per unit cell). Various outlying reflections (ca. 90) needed to be omitted for stable refinements. These resulted from low crystal quality, long exposure times (60 s) or were affected by the beam-stop.

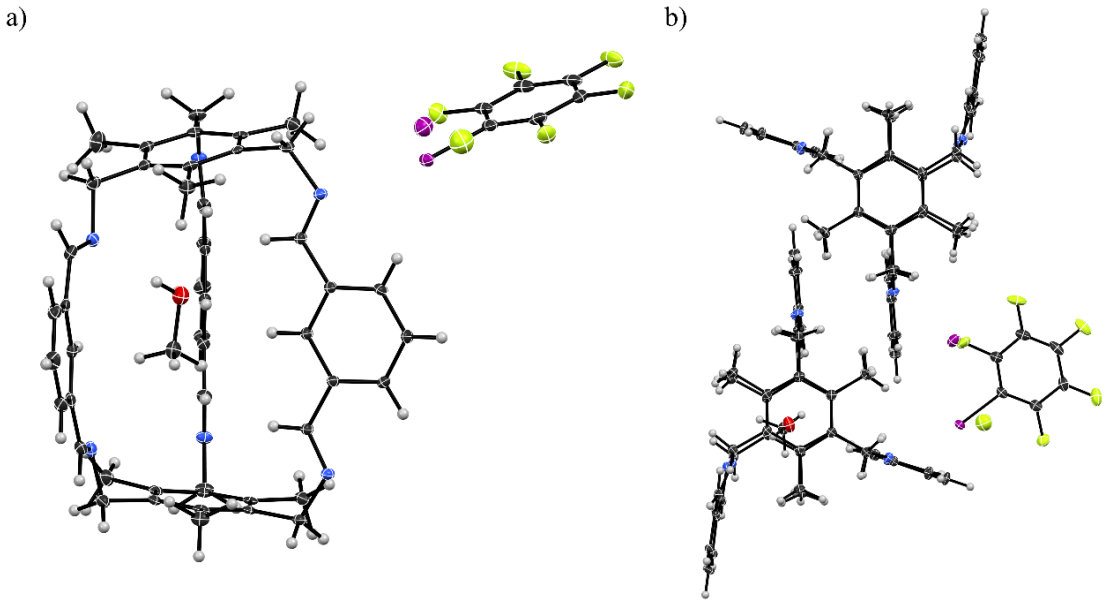

Figure S3: Data set of **A···IF_5** showing a), the asymmetric unit bearing one cage **A** and one **IF_5** molecule, together with an ordered methanol solvent molecule, thermal ellipsoids set at 50 % probability. The iodine atom shows positional disorder (88:12), which was treated accordingly, which is also visible in b), please see Table S4 for both possible halogen bonding interactions.

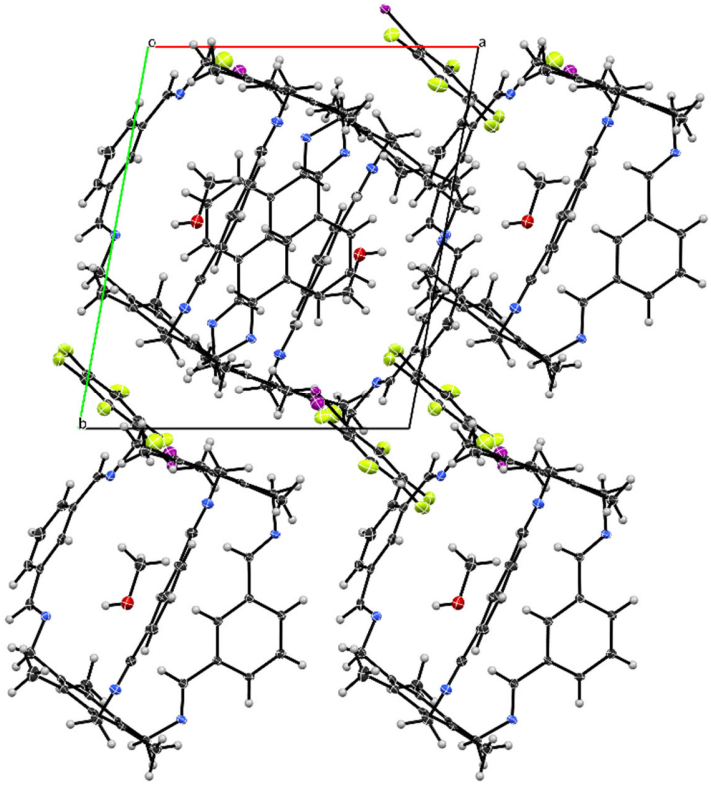

Figure S4: View of the extended unit cell of **A···IF$_5$** along the crystallographic *c* axis.

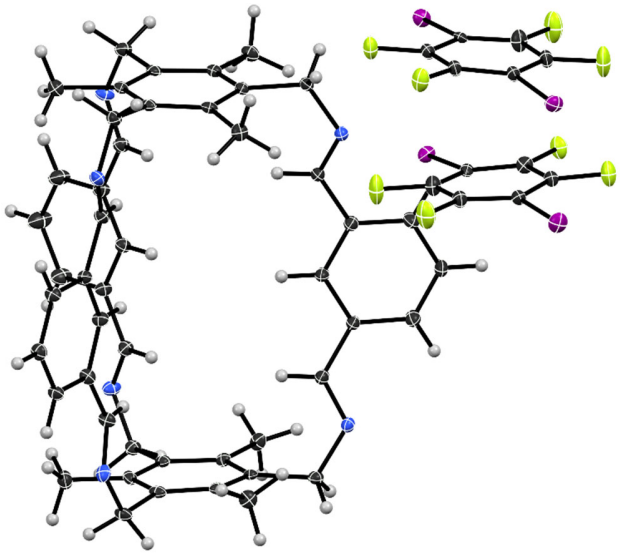

Figure S5: Data set of **A···2(I$_2$F$_4$)** showing the asymmetric unit bearing one cage **A** and two **I$_2$F$_4$** molecules, thermal ellipsoids set at 50 % probability, one disordered chloroform molecule was omitted for clarity.

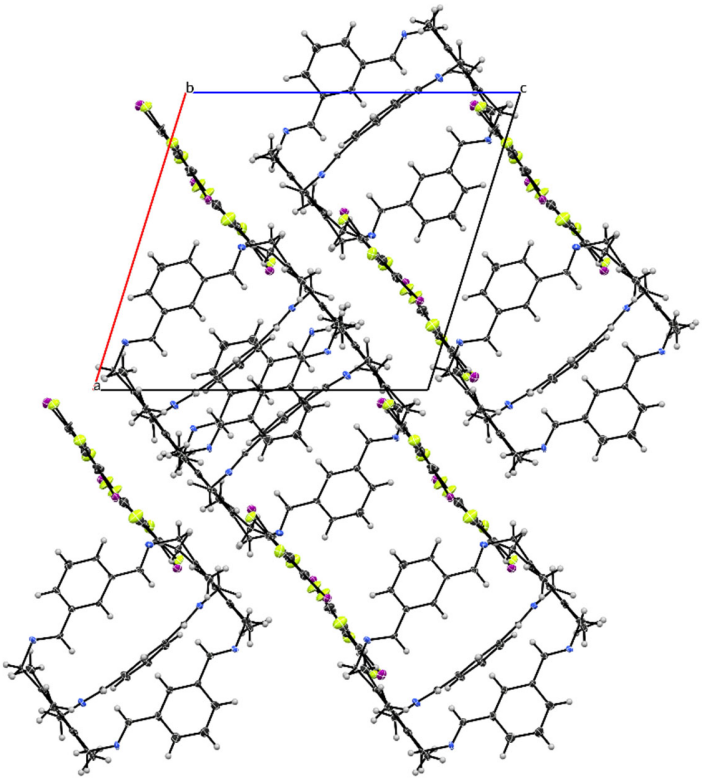

Figure S6: View of the extended unit cell of **A···2(I_2F_4)** along the crystallographic *b* axis, with solvent molecules omitted for clarity.

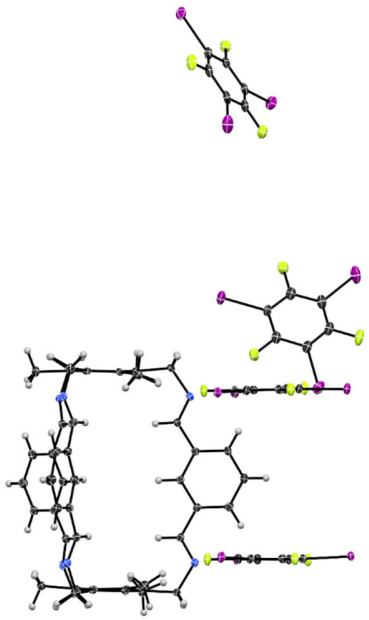

Figure S7: Data set of **A···4(I_3F_3)** showing the asymmetric unit bearing one cage **A** and four I_3F_3 molecules, thermal ellipsoids set at 50 % probability.

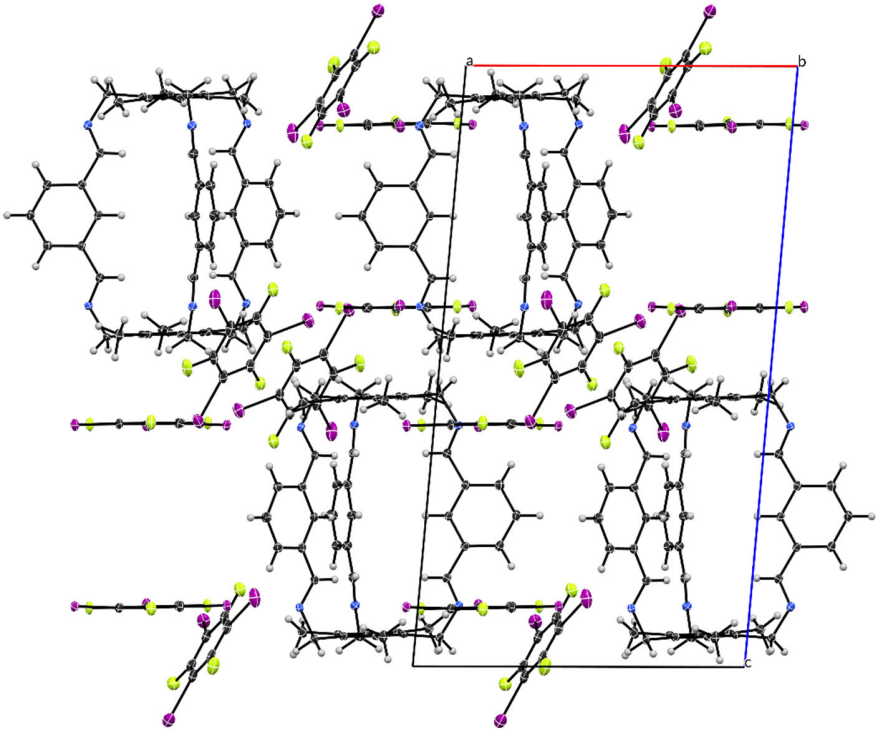

Figure S8: View of the extended unit cell of **A···4(I_3F_3)** along the crystallographic *b* axis.

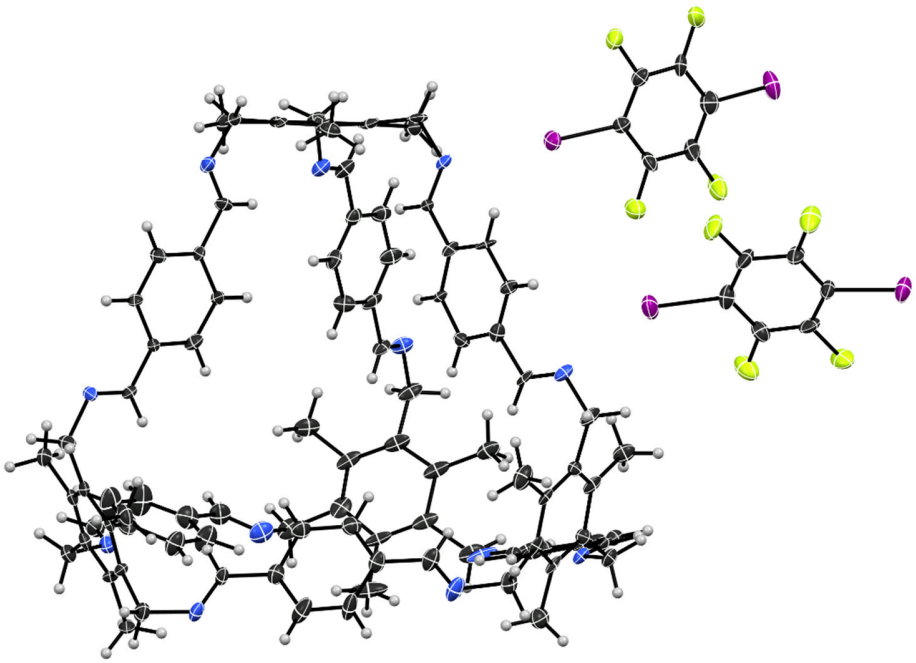

Figure S9: Data set of **B···2(I_2F_4)** showing the asymmetric unit bearing one cage and two I_2F_4 molecules, thermal ellipsoids set at 50 % probability.

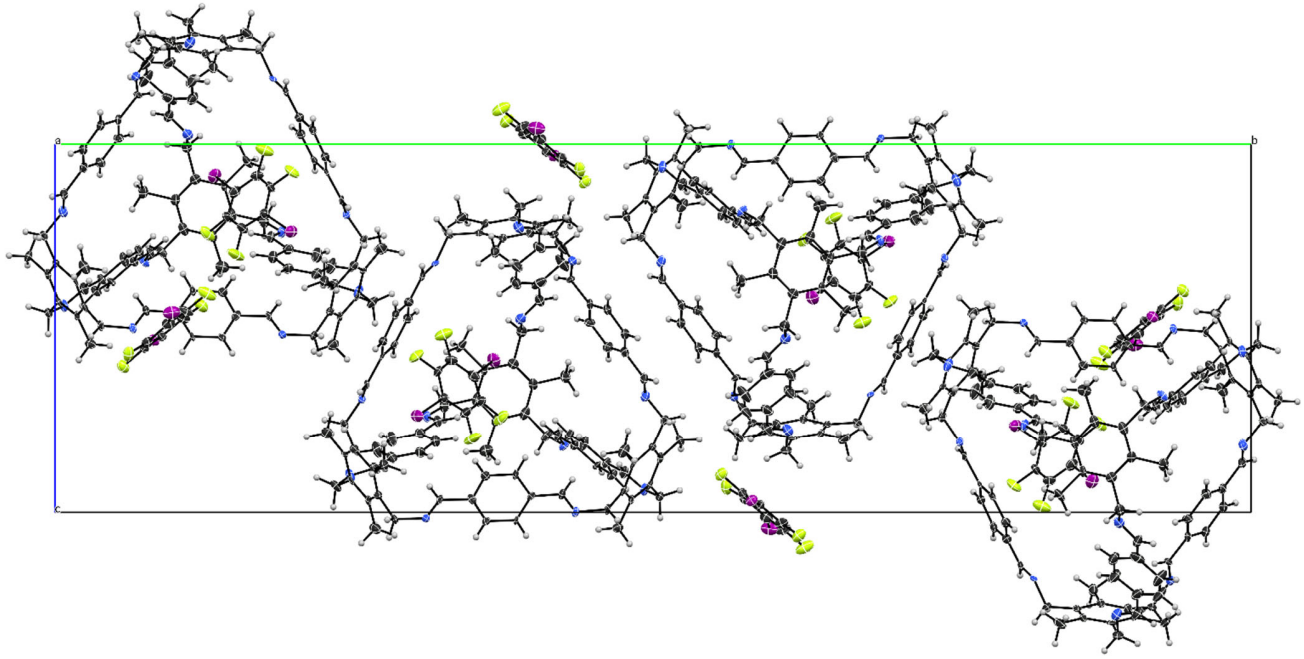

Figure S10: View of the unit cell of **B···2(I_2F_4)** along the crystallographic *a* axis.

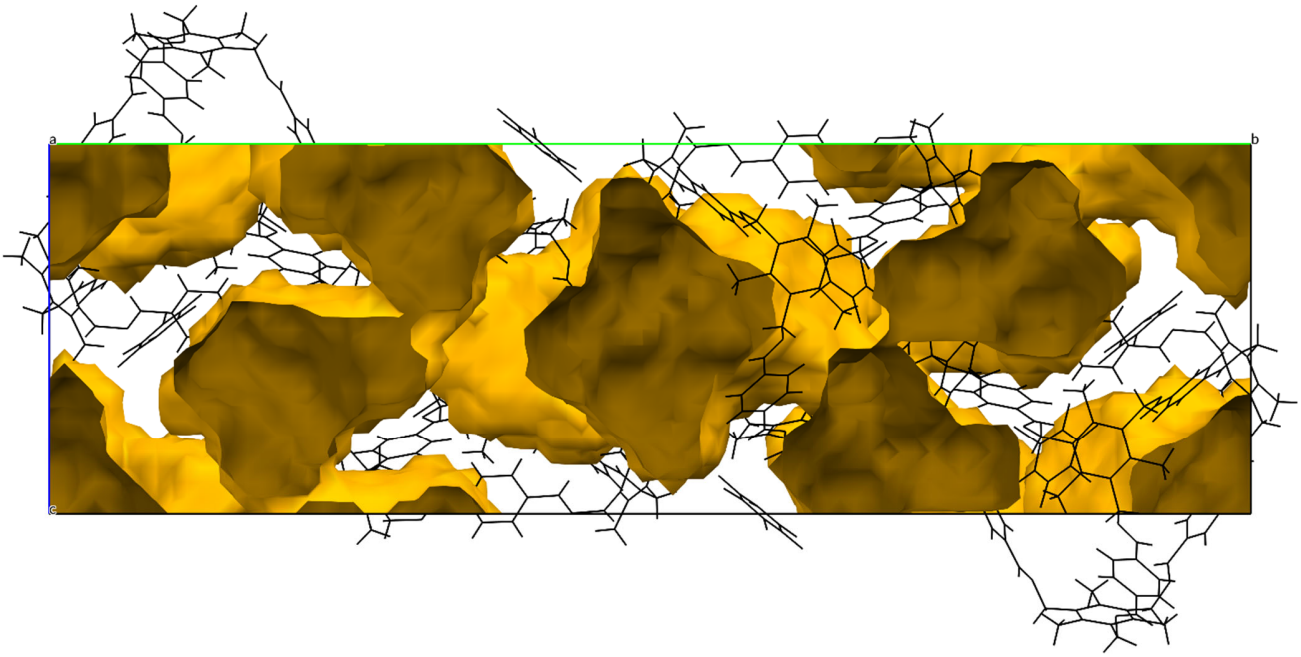

Figure S11: View of the unit cell of **B···2(I_2F_4)** along the crystallographic *a* axis, voids calculated using a probe of 1.2 Å and depicted in orange colour.

Table S2: Crystal structure refinement details for **A···IF_5** and **A···2(I_2F_4)**.

	A···IF_5	**A···2(I_2F_4)**
Wavelength [Å]	Mo Kα	Mo Kα
Collection Temperature [K]	153	100
Formula	$C_{55}H_{52}F_5IN_6O$	$C_{61}H_{49}Cl_3F_8I_4N_6$
Formula weight	1034.92	1632.01
Crystal System	Triclinic	Triclinic
Space Group	P-1	P-1
a [Å]	12.0972(18)	14.6891(4)
b [Å]	15.049(3)	15.0515(2)
c [Å]	15.5995(18)	15.8495(4)
α [°]	116.465(5)	96.972(2)
β [°]	108.720(5)	106.882(2)
γ [°]	90.484(7)	91.054(2)
V [$Å^3$]	2369.1(6)	3323.09(14)
Z	2	2
μ [mm^{-1}]	0.74	2.06
Crystal size [mm]	0.15 x 0.14 x 0.11	0.46 x 0.24 x 0.18
Reflections collected	80779	17048
Independent reflections	9695	17048
Observed reflections [$I > 2\sigma(I)$]	7992	13997
R_{int}	0.089	-
Data/ parameters/restraints	9695/640/10	17048/786/267
$R[F^2>2\sigma(F^2)]$	0.037	0.056
$wR(F^2)$	0.079	0.167

Table S3: Crystal structure refinement details for **A⋯4(I_3F_3)** and **B⋯2(I_2F_4)**.

	A⋯4(I_3F_3)	**B⋯2(I_2F_4)**
Wavelength [Å]	Mo Kα	Mo Kα
Collection Temperature [K]	100	153
Formula	$C_{72}H_{48}F_{12}I_{12}N_6$	$C_{108}H_{95}F_8I_4N_{12}$
Formula weight	2747.96	2220.55
Crystal System	Triclinic	Monoclinic
Space Group	P-1	$P2_{1/c}$
a [Å]	15.1876(3)	13.882(1)
b [Å]	15.3098(2)	55.671(4)
c [Å]	23.9698(4)	17.1632(12)
α [°]	89.922(1)	
β [°]	85.674(1)	91.325(2)
γ [°]	60.309(2)	
V [$Å^3$]	4823.73(16)	13260.5(17)
Z	2	4
μ [mm^{-1}]	3.91	0.99
Crystal size [mm]	0.33 x 0.27 x 0.19	0.19 x 0.17 x 0.04
Reflections collected	89851	178104
Independent reflections	25176	23276
Observed reflections [$I > 2\sigma(I)$]	20622	15995
R_{int}	0.036	0.087
Data/ parameters/restraints	25176/925	23276/1201/30
$R[F^2>2\sigma(F^2)]$	0.039	0.097
$wR(F^2)$	0.088	0.272

Table S4: Bond lengths [Å] and angles [°] for **A⋯IF_5**.

I(10)-N(11)	3.023(2)	N⋯I halogen bond
I(10A)-N(20)	3.043(4)	N⋯I halogen bond
N(31)-H(200)	2.234	hydrogen bonding
F(11)-H(19B)	2.968	H⋯F contact
F(12)-H(36)	2.646	H⋯F contact
F(12)-H(37)	2.629	H⋯F contact
F(13)-H(9AB)	2.662	H⋯F contact
F(13)-H(39A)	2.732	H⋯F contact
F(14)-H(8AA)	2.982	H⋯F contact
F(15)-H(31)	2.824	H⋯F contact
$Centroid_{(C1,2,3,4,5,6)}$-$Centroid_{(C1,2,3,4,5,6)}$	4.012	π-stacking (cage-cage)
$Centroid_{(C1A,2A,3A,4A,5A,6A)}$-$Centroid_{(C100,101,102,103,104,105)}$	3.653	π-stacking (cage-donor)
$Centroid_{(C12,13,14,15,16,17)}$- $Centroid_{(C12,13,14,15,16,17)}$	4.082	π-stacking (cage-cage)
$Centroid_{(C22,23,24,25,26,27)}$-$Centroid_{(C22,23,24,25,26,27)}$	3.729	π-stacking (cage-cage)
$Centroid_{(C100,101,102,103,104,105)}$- $Centroid_{(C100,101,102,103,104,105)}$	3.569	π-stacking (donor-donor)

C(100)-I(10)-N(11)	166.17(9)	N···I halogen bond
C(101)-I(10A)-N(20)	162.9(3)	N···I halogen bond
O(200)-H(200)-N(31)	173.6	hydrogen bonding
C(101)-F(11)-H(19B)	74.8	H···F contact
C(102)-F(12)-H(36)	127.6	H···F contact
C(102)-F(12)-H(37)	148.1	H···F contact
C(103)-F(13)-H(9AB)	82.6	H···F contact
C(103)-F(13)-H(39A)	97.4	H···F contact
C(104)-F(14)-H(8AA)	120.8	H···F contact
C(105)-F(15)-H(31)	149.8	H···F contact

Table S5: Bond lengths [Å] and angles [°] for **A···2(I_2F_4)**.

I(1)-N(6)	2.997(5)	N···I halogen bond
I(2)-N(1)	2.953(4)	N···I halogen bond
I(3)-N(5)	2.933(3)	N···I halogen bond
I(4)-N(3)	2.980(4)	N···I halogen bond
F(1)-H(23B)	3.047	H···F contact (inner layer)
F(1)-H(28)	2.634	H···F contact (inner layer)
F(1)-H(48C)	3.042	H···F contact (inner layer)
F(2)-H(23A)	2.882	H···F contact (inter layer)
F(2)-H(43)	3.063	H···F contact (inner layer)
F(2)-H(48C)	2.954	H···F contact (inner layer)
F(3)-H(19B)	3.011	H···F contact (inter layer)
F(4)-H(49C)	3.068	H···F contact (inter layer)
F(5)-H(11B)	3.085	H···F contact (inter layer)
F(6)-H(52B)	2.895	H···F contact (inter layer)
F(7)-H(7A)	3.120	H···F contact (inner layer)
F(7)-H(26)	2.616	H···F contact (inner layer)
F(7)-H(50B)	3.074	H···F contact (inner layer)
F(7)-H(50C)	2.682	H···F contact (inter layer)
F(8)-H(7A)	3.025	H···F contact (inter layer)
F(8)-H(45)	3.042	H···F contact (inner layer)
F(8)-H(50B)	2.992	H···F contact (inner layer)
$Centroid_{(C8,9,10,29,30,31)}$-$Centroid_{(C58,59,60,61,62,63)}$	3.731	π-stacking (donor-cage)
$Centroid_{(C14,15,16,53,54,55)}$- $Centroid_{(C14,15,16,53,54,55)}$	3.724	π-stacking (cage-cage)
$Centroid_{(C20,21,22,41,42,46)}$-$Centroid_{(C12,24,33,39,56,57)}$	3.844	π-stacking (donor-cage)
$Centroid_{(C35,36,37,43,44,45)}$- $Centroid_{(C35,36,37,43,44,45)}$	4.020	π-stacking (cage-cage)
C(12)-I(1)-N(6)	168.6(2)	N···I halogen bond
C(39)-I(2)-N(1)	165.0(2)	N···I halogen bond
C(58)-I(3)-N(5)	164.6(2)	N···I halogen bond
C(61)-I(4)-N(3)	171.6(2)	N···I halogen bond
C(56)-F(1)-H(23B)	151.4	H···F contact (inner layer)
C(56)-F(1)-H(28)	113.5	H···F contact (inner layer)

C(56)-F(1)-H(48C)	124.1	H···F contact (inner layer)
C(57)-F(2)-H(23A)	103.1	H···F contact (inter layer)
C(57)-F(2)-H(43)	128.7	H···F contact (inner layer)
C(57)-F(2)-H(48C)	127.0	H···F contact (inner layer)
C(24)-F(3)-H(19B)	71.9	H···F contact (inter layer)
C(33)-F(4)-H(49C)	98.6	H···F contact (inter layer)
C(62)-F(5)-H(11B)	99.4	H···F contact (inter layer)
C(63)-F(6)-H(H52B)	78.8	H···F contact (inter layer)
C(59)-F(7)-H(7A)	152.1	H···F contact (inner layer)
C(59)-F(7)-H(26)	113.0	H···F contact (inner layer)
C(59)-F(7)-H(50B)	124.2	H···F contact (inner layer)
C(59)-F(7)-H(50C)	104.2	H···F contact (inter layer)
C(60)-F(8)-H(7A)	122.9	H···F contact (inter layer)
C(60)-F(8)-H(45)	130.3	H···F contact (inner layer)
C(60)-F(8)-H(50B)	127.2	H···F contact (inner layer)

Table S6: Bond lengths [Å] and angles [°] for **A···4(I_3F_3)**.

I(1)-N(53)	2.972(5)	N···I halogen bond
I(2)-N(77)	3.016(4)	N···I halogen bond
I(3)-N(71)	2.967(5)	N···I halogen bond
I(19)-N(83)	2.994(4)	N···I halogen bond
I(20)-N(59)	2.978(5)	N···I halogen bond
I(21)-N(65)	3.004(4)	N···I halogen bond
I(3)-I(6)	3.8229(6)	I···I halogen bond
I(9)-I(20)	3.8433(5)	I···I halogen bond
F(10)-H(76B)	3.028	H···F contact
F(11)-H(98C)	2.946	H···F contact
F(12)-H(72A)	3.074	H···F contact
F(22)-H(95C)	2.942	H···F contact
F(23)-H(64A)	3.078	H···F contact
F(24)-H(60B)	3.066	H···F contact
F(46)-H(84A)	2.706	H···F contact
F(48)-H(60A)	2.671	H···F contact
$Centroid_{(C1,2,3,4,5,6)}$-$Centroid_{(C49,50,51,73,74,75)}$	3.785	π-stacking (cage-donor)
$Centroid_{(C13,14,15,16,17,18)}$-$Centroid_{(C61,62,63,85,86,93)}$	3.767	π-stacking (cage-donor)
$Centroid_{(C25,26,27,28,29,30)}$-$Centroid_{(C25,26,27,28,29,30)}$	3.657	π-stacking (donor-donor)
$Centroid_{(C37,38,39,40,41,42)}$-$Centroid_{(C37,38,39,40,41,42)}$	3.624	π-stacking (donor-donor)
C(3)-I(1)-N(53)	166.3(1)	N···I halogen bond
C(5)-I(2)-N(77)	164.7(1)	N···I halogen bond
C(1)-I(3)-N(71)	165.9(2)	N···I halogen bond
C(13)-I(19)-N(83)	165.5(1)	N···I halogen bond
C(15)-I(20)-N(59)	166.4(1)	N···I halogen bond
C(17)-I(21)-N(65)	163.5(1)	N···I halogen bond
C(29)-I(6)-I(3)	160.9(1)	I···I halogen bond

C(41)-I(9)-I(20)	159.3(1)	I···I halogen bond
C(6)-F(10)-H(76B)	108.6	H···F contact
C(4)-F(11)-H(98C)	91.3	H···F contact
C(2)-F(12)-H(72A)	76.7	H···F contact
C(18)-F(22)-H(95C)	91.4	H···F contact
C(16)-F(23)-H(64A)	108.1	H···F contact
C(14)-F(24)-H(60B)	77.4	H···F contact
C(42)-F(46)-H(84A)	82.5	H···F contact
C(38)-F(48)-H(60A)	138.7	H···F contact

Table S7: Bond lengths [Å] and angles [°] for **B···2(I_2F_4)**.

I(200)-N(51)	2.978(7)	N···I halogen bond
I(203)-centroid$_{C54,55}$	3.281	π···I halogen bond[S8]
I(300)-N(30)	3.251(9)	N···I halogen bond
I(303)-N(20)	3.448(7)	N···I contact
F(201)-H(49B)	2.550	H···F contact
F(205)-H(98B)	2.448	H···F contact
F(301)-H(43)	2.657	H···F contact
F(302)-H(53)	2.524	H···F contact
F(304)-H(69B)	2.520	H···F contact
Centroid$_{(C42,43,44,45,46,47)}$-Centroid$_{(200,201,202,203,204,205)}$	3.538	π-stacking (cage-donor)
C(200)-I(200)-N(51)	161.2(3)	N···I halogen bond
C(203)-I(203)-centroid$_{C54,55}$	171.32	π···I halogen bond
C(300)-I(300)-N(30)	164.6(3)	N···I halogen bond
C(303)-I(303)-N(20)	142.1(3)	N···I contact
C(201)-F(201)-H(49B)	122.0	H···F contact
C(205)-F(205)-H(98B)	152.0	H···F contact
C(301)-F(301)-H(43)	145.5	H···F contact
C(302)-F(302)-H(53)	132.6	H···F contact
C(304)-F(304)-H(69B)	140.9	H···F contact

Table S8: Bond lengths, sum of van der Waals Radii,[S9,S10] and normalized bond lengths for the halogen bonds in the different networks.

	Contact	d_{XB} [Å]	ΣBvdW (Bondi) [Å]	d_{XB}/ ΣBvdW	ΣBvdW (Rowland) [Å]	d_{XB}/ ΣBvdW
A···IF_5	N···I	3.023(2)	3.53	0.86	3.67	0.82
	N···I	3.043(4)	3.53	0.86	3.67	0.83
A···2(I_2F_4)	N···I	2.997(5)	3.53	0.85	3.67	0.82
	N···I	2.953(4)	3.53	0.84	3.67	0.80
	N···I	2.933(3)	3.53	0.83	3.67	0.80
	N···I	2.980(4)	3.53	0.84	3.67	0.81
A···4(I_3F_3)	N···I	2.972(5)	3.53	0.84	3.67	0.81
	N···I	3.016(4)	3.53	0.85	3.67	0.82
	N···I	2.967(5)	3.53	0.84	3.67	0.81
	N···I	2.994(4)	3.53	0.85	3.67	0.82
	N···I	2.978(5)	3.53	0.84	3.67	0.81
	N···I	3.004(4)	3.53	0.85	3.67	0.82
	I···I	3.8229(6)	3.96	0.97	4.06	0.94
	I···I	3.8433(5)	3.96	0.97	4.06	0.95
B···2(I_2F_4)	N···I	2.978(7)	3.53	0.84	3.67	0.81
	N···I	3.251(9)	3.53	0.92	3.67	0.89
	N···I	3.448(7)	3.53	0.98	3.67	0.94

V. Computational details

DFT-calculations were performed using QuantumEspresso[S11] for periodic crystals of **A···2(I_2F_4)**, **A···4(I_3F_3)** and **B···2(I_2F_4)**. Gaussian16[S12] was used for the simplified model systems 1 and 2 in vacuum. The unit-cell structures of **A···2(I_2F_4)**, **A···4(I_3F_3)** and **B···2(I_2F_4)** were geometry-optimized using the Broyden-Fletcher-Goldfarb-Shanno (BFGS) scheme using the experimentally obtained unit cells as starting configuration. Atoms were described with ultrasoft Rappe-Rabe-Kaxiras-Joannopoulos(RRKJ)-type pseudopotentials. Periodic plane-wave DFT computations were performed using the generalized gradient approximation (GGA) with Perdew-Burke-Enzerhof (PBE) exchange correlation and the Monkhorst pack scheme with a 2 x 2 x 2 k-point mesh for **A···2(I_2F_4)** and **A···4(I_3F_3)** structures. The unit cell of **B···2(I_2F_4)** was evaluated using only the Γ-point. An energy cutoff of 70 Rydberg and a charge cutoff of 700 Rydberg was applied. To account for dispersion effects, the semi-empirical Grimme D3-correction scheme[S13] was adopted. For QTAIM-analysis, a single point computation on the optimized structures was performed using CP2K[S14] with the DZVP-MOLOPT-GTH basis set and corresponding GTH-PBE pseudopotentials.

Model 1 was created from the optimized structure of **A···2(I_2F_4)** by cutting the cages to keep two bis-aminomethyl-benzenes that bind two **I_2F_4** donors. Both model 1 and 2 structures were geometry-optimized in vacuo with the M062X density functional[S15] and the CEP-121G basis set. The nature of stationary points was verified through vibrational analysis yielding no imaginary frequencies. Wavefunction analysis was performed for all computed structures with Multiwfn.[S16] Approximate interaction energies between halogen-bond donor and acceptor atoms were obtained by a) computing the kinetic energy density $\beta \cdot G(r)$ and b) by calculating the potential energy density $-\gamma \cdot V(r)$ of the electrons at the X-B bond critical point. Here, the coefficients β and γ denote proportionality factors. Tables S9 and S10 list interaction energies computed with the proportionality coefficients used by Espinosa et al. (β=0.429, γ=0.5)[S17,S18] and atom specific parameters reported by Bartashevich and Tsirelson (β=0.67, γ=0.68).[S19]

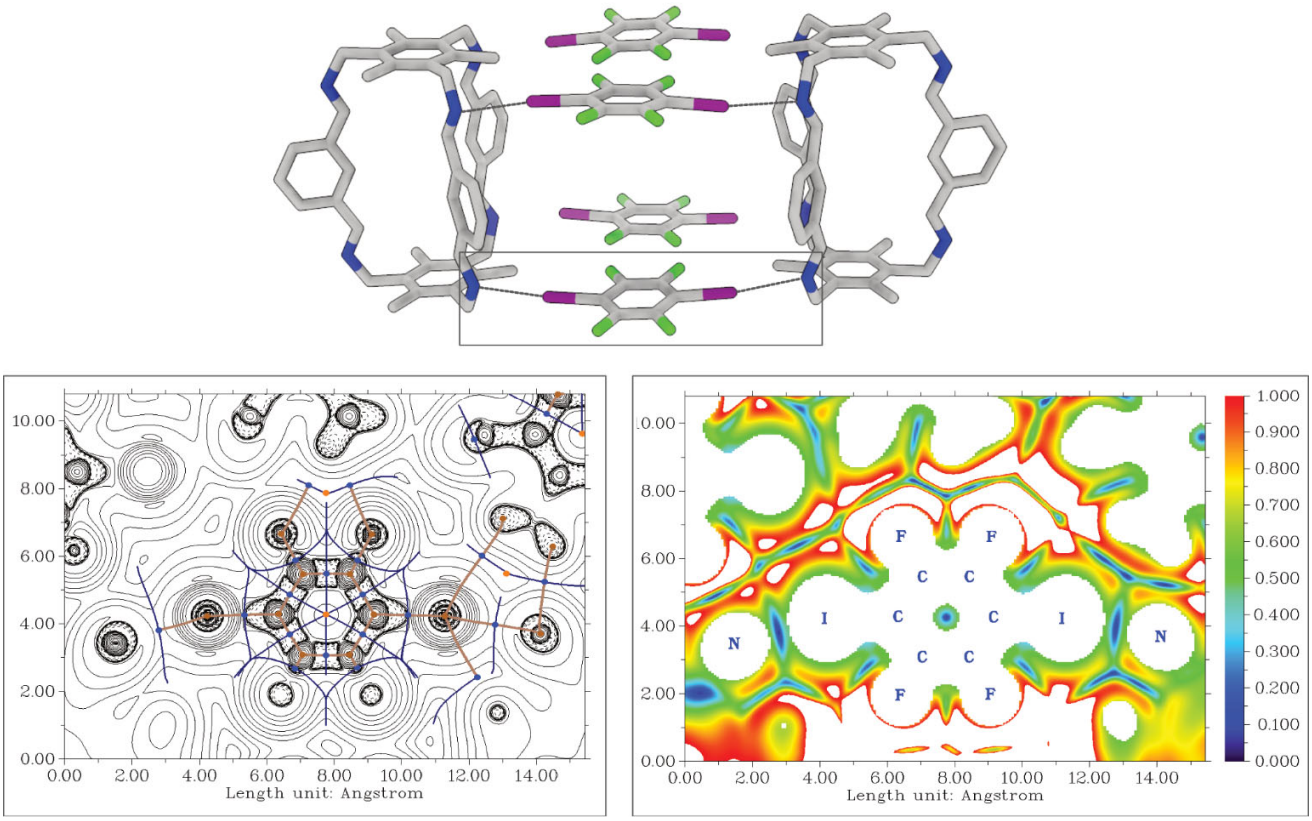

Figure S12: Structure of **A···2(I_2F_4)**. Laplacian map of the electron density (left) is depicted with critical points and bond paths. Bond critical (3,-1) points in blue, nuclear critical (3,-3) points in brown, ring critical (3,+1) points in orange, paths and zero-flux surfaces as brown and blue lines. The reduced density gradient map is shown on the right side.

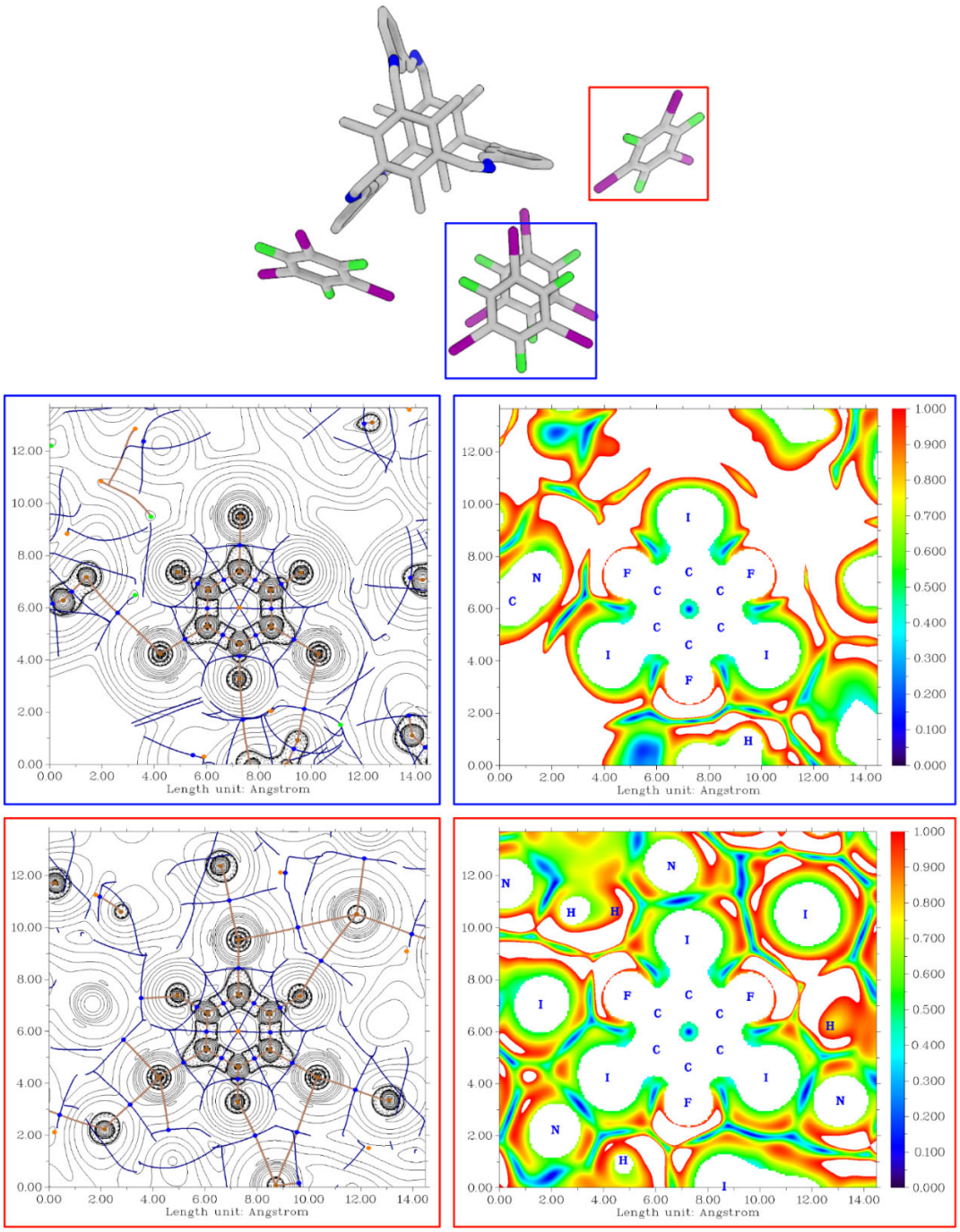

Figure S13: Structure of **A···4(I_3F_3)** including the I_3F_3 interconnecting the cages (blue outline) and the I_3F_3 showing "solvent-like" behaviour (red outline). Laplacian maps of the electron density (left) are depicted with critical points and bond paths. Bond critical (3,-1) points in blue, nuclear critical (3,-3) points in brown, ring critical (3,+1) points in orange, paths and zero-flux surfaces as brown and blue lines. The reduced density gradient maps are shown on the right side.
Blue: Laplacian and reduced gradient maps for of **A···4(I_3F_3)** with I_3F_3 showing "solvent-like" behaviour.
Red: Laplacian and reduced gradient maps for of **A···4(I_3F_3)** with I_3F_3 interconnecting the cages.

Table S9: Distances and interaction energies (kJ/mol) in **A···2(I_2F_4)** and **A···4(I_3F_3)**.

Model	Bond	Distance [Å]	0.429·G(r)	-0.5·V(r)	0.67·G(r)	-0.68·V(r)
A···2(I_2F_4)$_{XB}$	I-N (1)	2.89	15.64	17.19	24.43	23.37
	I-N (2)	2.84	17.66	19.97	27.58	27.16
A···4(I_3F_3)$_{XB}$	I-N (1)	2.91	15.16	16.39	23.68	22.29
	I-N (2)	2.90	15.51	16.97	24.22	23.08
	I-N (3)	2.93	14.45	15.50	22.60	21.08
A···4(I_3F_3)$_{comp}$	I-N	4.07	2.02	1.66	3.16	2.26
	F-N	3.38	2.53	1.97	3.95	2.67
	I-H	3.39	2.53	2.12	3.96	2.89
	I-I (1)	3.86	4.74	4.40	7.39	5.98
	I-I (2)	4.48	2.12	1.76	3.31	2.40
	I-I (3)	4.67	1.46	1.13	2.28	1.54

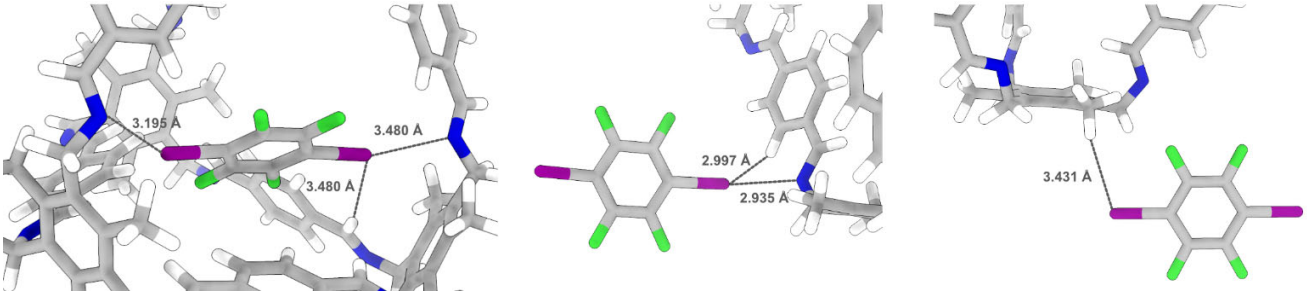

Figure S14: Binding modes of **I_2F_4** inside and outside cage.

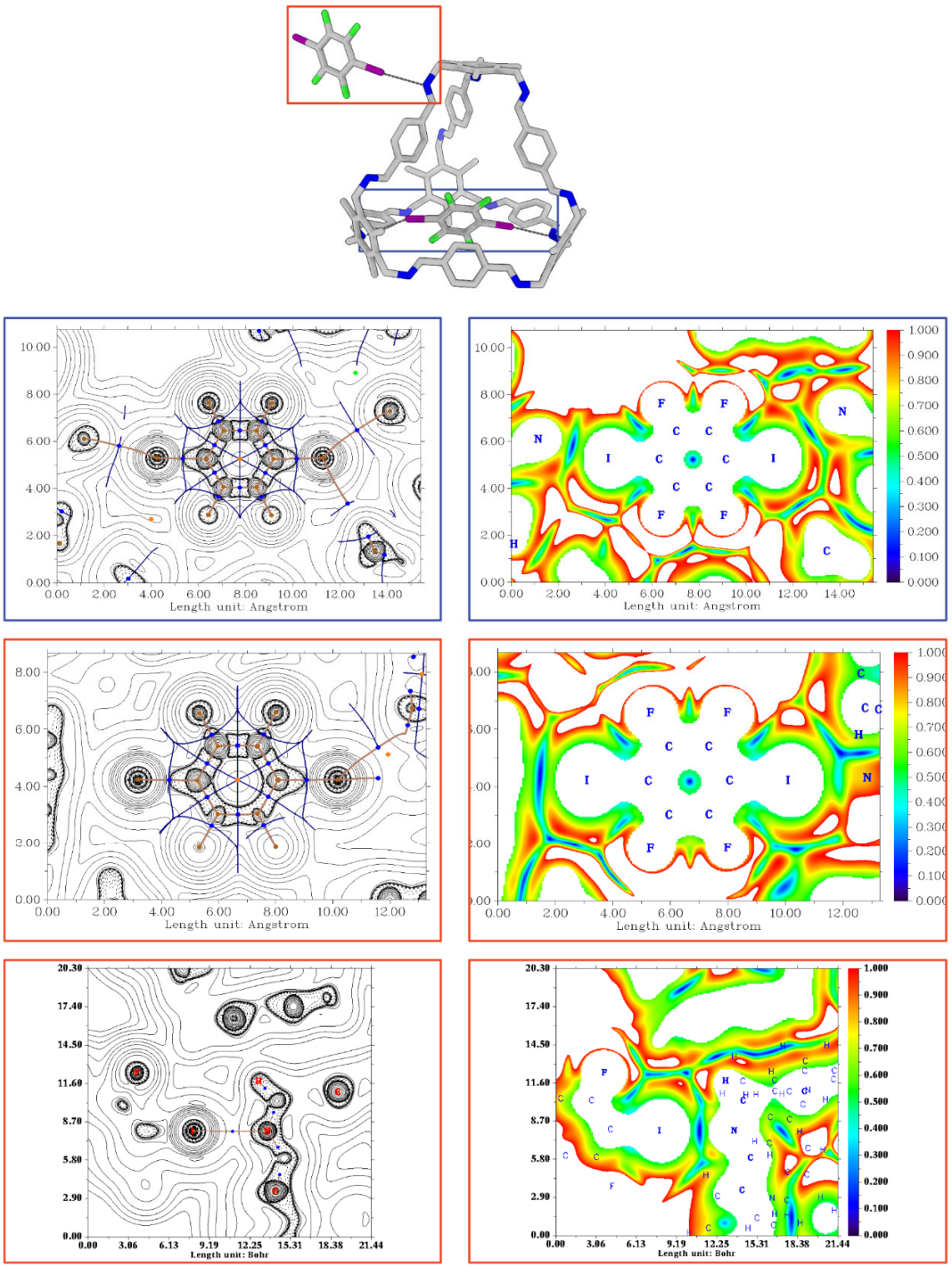

Figure S15: Structure of **B···2(I_2F_4)** including the I_2F_4 located inside the cage (red outline) and the I_2F_4 located on the outside (blue outline). Laplacian maps of the electron density (left) are depicted with critical points and bond paths. Bond critical (3,-1) points in blue, nuclear critical (3,-3) points in brown, ring critical (3,+1) points in orange, paths and zero-flux surfaces as brown and blue lines. The reduced density gradient maps are shown on the right side.
Blue: Laplacian and reduced gradient maps for **B···2(I_2F_4)** with I_2F_4 inside cage.
Red: Laplacian and reduced density gradient map of **B···2(I_2F_4)** with I_2F_4 outside cage showing the whole donor (depicted along the ring plane, upper section) and the imine halogen bond (shown along the I···N bond axis, lower section). Zero-flux surfaces were omitted in the latter.

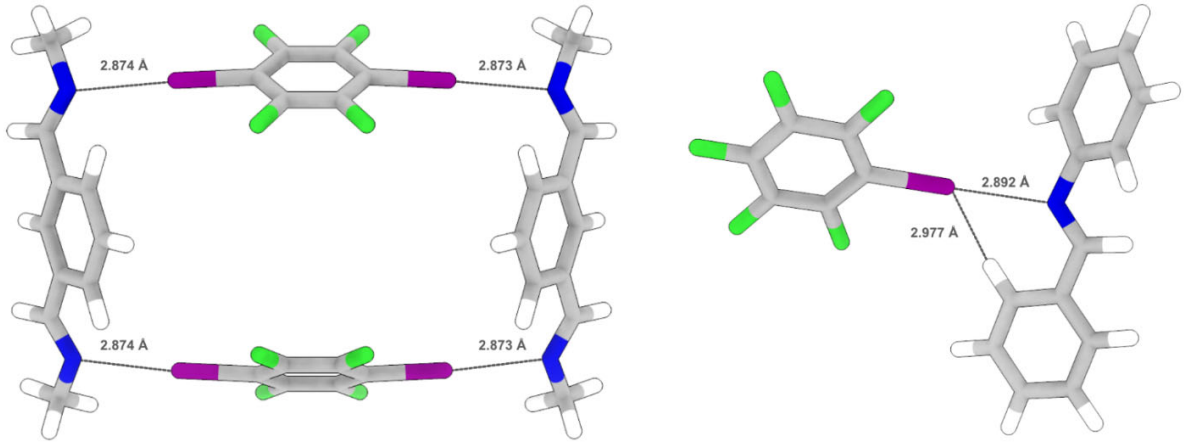

Figure S16: Binding modes of I_2F_4 in model 1 (left) and of IF_5 model 2 (right).

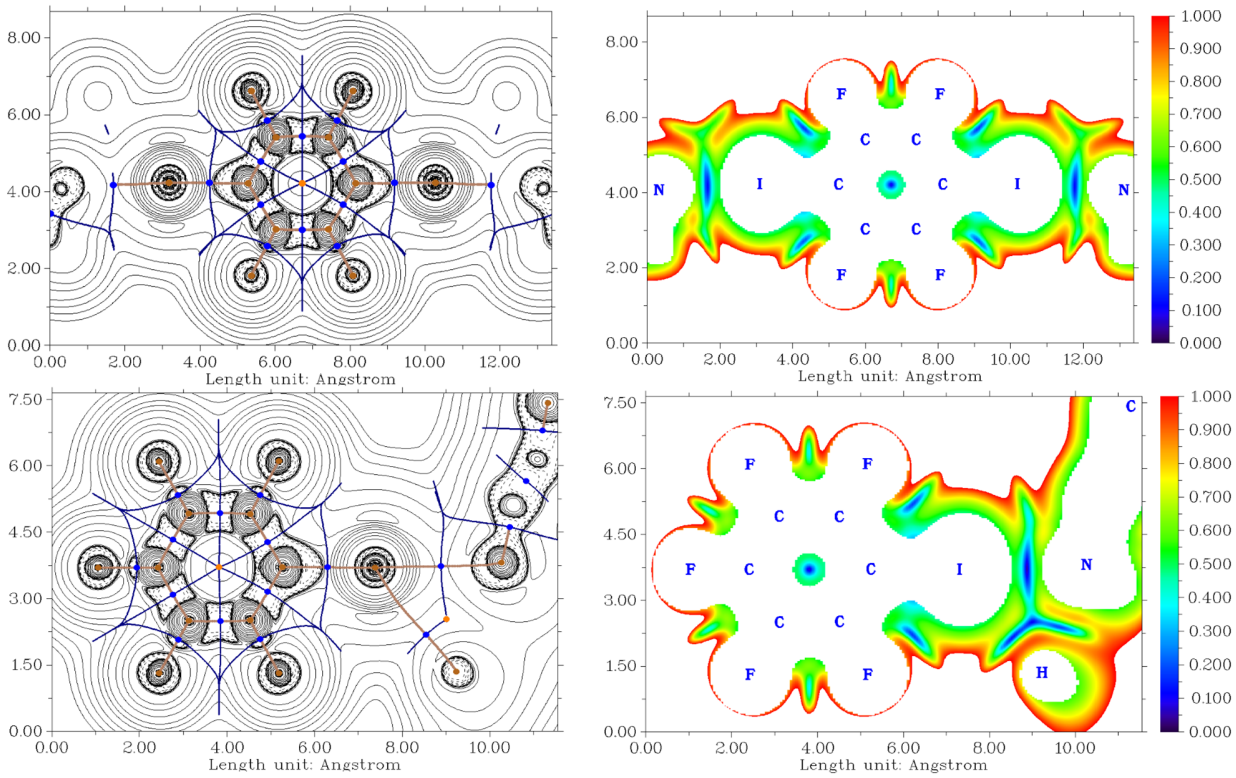

Figure S17: Left: Laplacian of electron density with critical points and bond paths. Bond critical (3,-1) points in blue, nuclear critical (3,-3) points in brown, ring critical (3,+1) points in orange, paths and zero-flux surfaces as brown and blue lines. Right: reduced density gradient map denoting halogen bonds in models 1 (upper section) and 2 (lower section).

Table S10: Distances and binding energies (kJ/mol) in **B···2(I_2F_4)** and in models 1 and 2.

Model	Bond	Distance [Å]	0.429·G(r)	-0.5·V(r)	0.67·G(r)	-0.68·V(r)
B···2(I_2F_4)$_{XB(ext)}$	I-N	2.94	14.59	15.78	22.78	21.45
	I-H	3.00	5.96	5.46	9.31	7.43
B···2(I_2F_4)$_{external}$	I-H	3.43	2.58	2.17	4.02	2.95
B···2(I_2F_4)$_{cage}$	I-N(1)	3.20	8.55	8.37	13.35	11.39
	I-N(2)	3.48	5.23	4.85	8.13	6.60
	I-H	3.48	2.11	1.76	3.30	2.39
model 1$_{XB}$	I-N	2.87	19.63	21.57	30.65	29.33
model 2$_{XB}$	I-N	2.89	18.62	20.15	29.07	27.41
	I-H	3.00	5.98	5.40	9.34	7.34

VI. Powder X-ray diffraction (PXRD) measurements

PXRD measurements were obtained using a Rigaku Miniflex 600 with Cu-K_α radiation (40 kV, 15mA). The samples were measured at 2θ angles from 5-50 °. The most intense reflection in each diffractogram was normalized to 1 for better visibility.

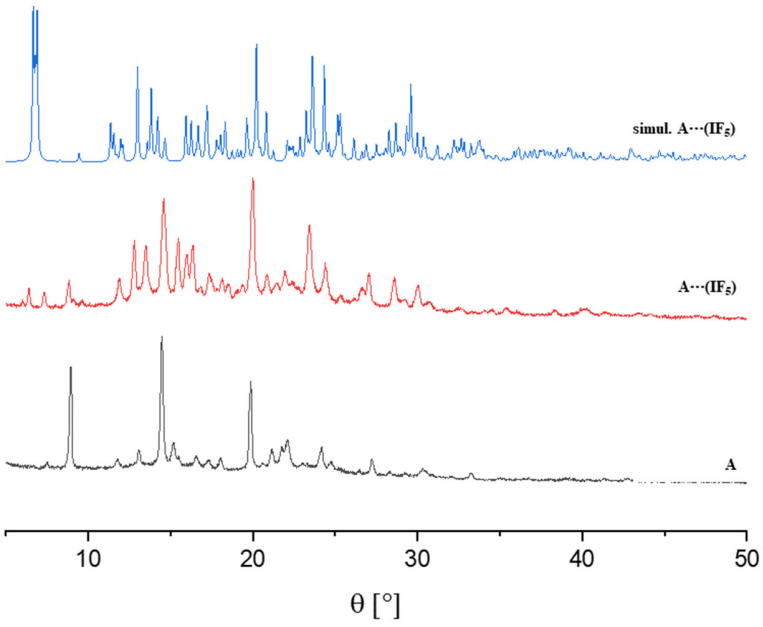

Figure S18: Simulated diffractogram of **A···IF$_5$** (blue) obtained by using the SXRD data and measured powder X-ray diffractograms of **A···IF$_5$** (red) and **A** (grey).

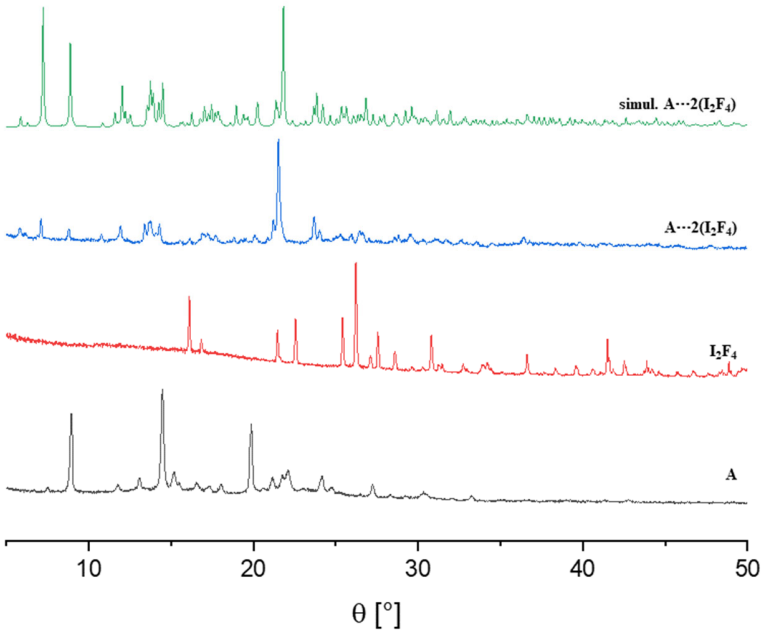

Figure S19: Simulated diffractogram of **A···2(I_2F_4)** (green) obtained by using the SXRD data and measured powder X-ray diffractograms of **A···2(I_2F_4)** (blue), **I_2F_4** (red) and **A** (grey).

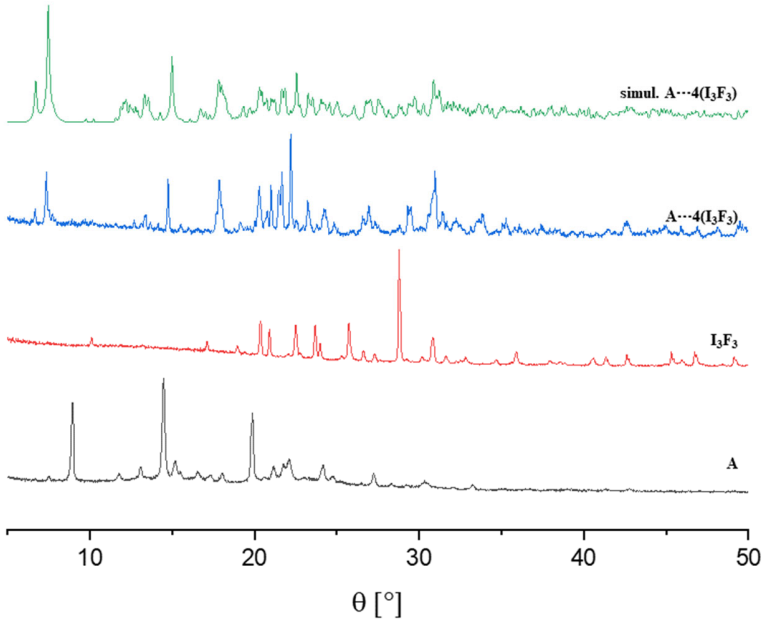

Figure S20: Simulated diffractogram of **A···4(I_3F_3)** (green) obtained by using the SXRD data and measured powder X-ray diffractograms of **A···4(I_3F_3)** (blue), **I_3F_3** (red) and **A** (grey).

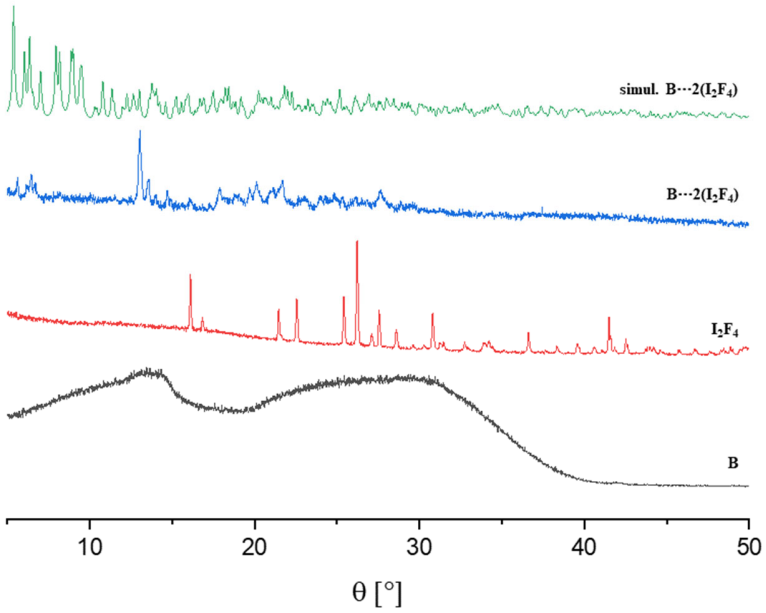

Figure S21: Simulated diffractogram of **B···2(I_2F_4)** (green) obtained by using the SXRD data and measured powder X-ray diffractograms of **B···2(I_2F_4)** (blue), **I_2F_4** (red) and **B** (grey).

VII. IR analysis

Infrared spectra were recorded with a Shimadzu IR Affinity-1 with ATR sampling technique. Crystalline samples were prepared as mentioned above. The spectra were standardized for better comparability.

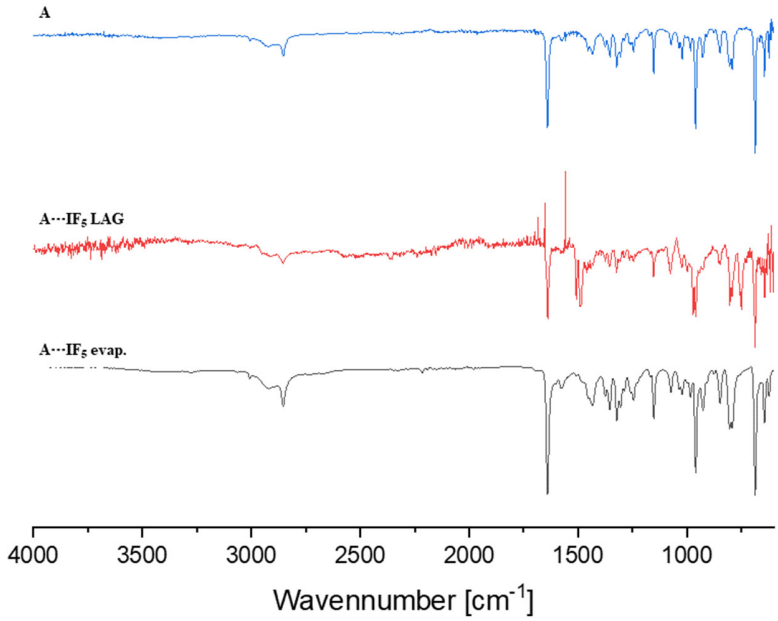

Figure S22: Measured IR-spectra of acceptor **A** (blue), **A···IF$_5$** synthesized by liquid assisted grinding (red) and **A···4(IF$_5$)** obtained by slow evaporation (grey).

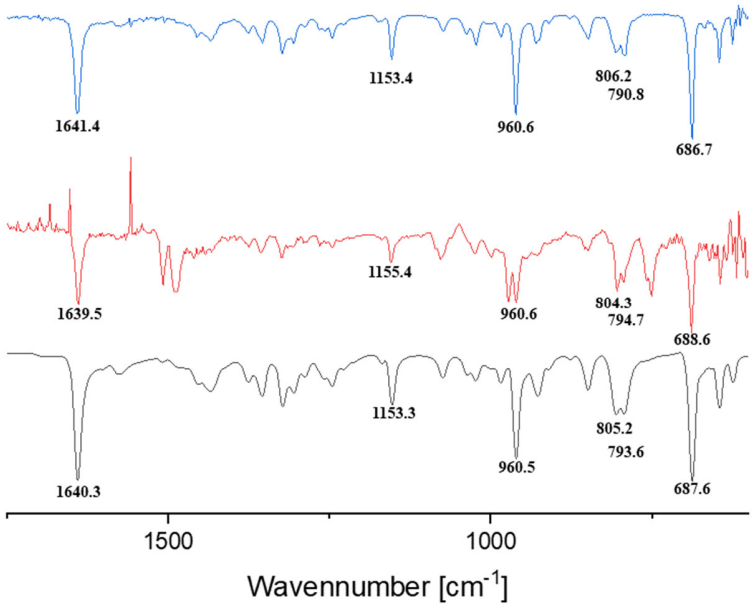

Figure S23: Enlarged detail of the measured IR-spectra of acceptor **A** (blue), **A···4(IF$_5$)** synthesized by liquid assisted grinding (red) and **A···4(IF$_5$)** obtained by slow evaporation (grey).

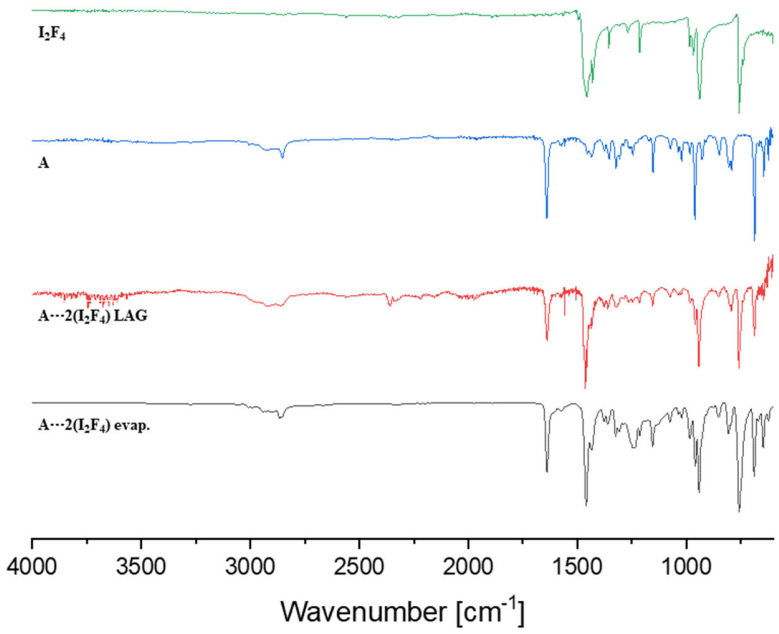

Figure S24: Measured IR-spectra of **I_2F_4** (green), acceptor **A** (blue), **A···2(I_2F_4)** synthesized by liquid assisted grinding (red) and **A···2(I_2F_4)** obtained by slow evaporation (grey).

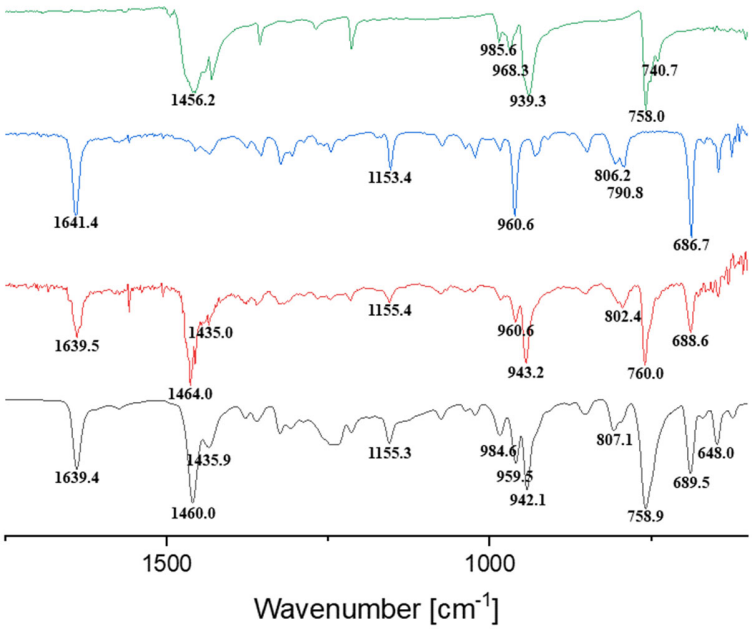

Figure S25: Enlarged detail of the measured IR-spectra of **I_2F_4** (green), acceptor **A** (blue) **A···2(I_2F_4)** synthesized by liquid assisted grinding (red) and **A···2(I_2F_4)** obtained by slow evaporation (grey).

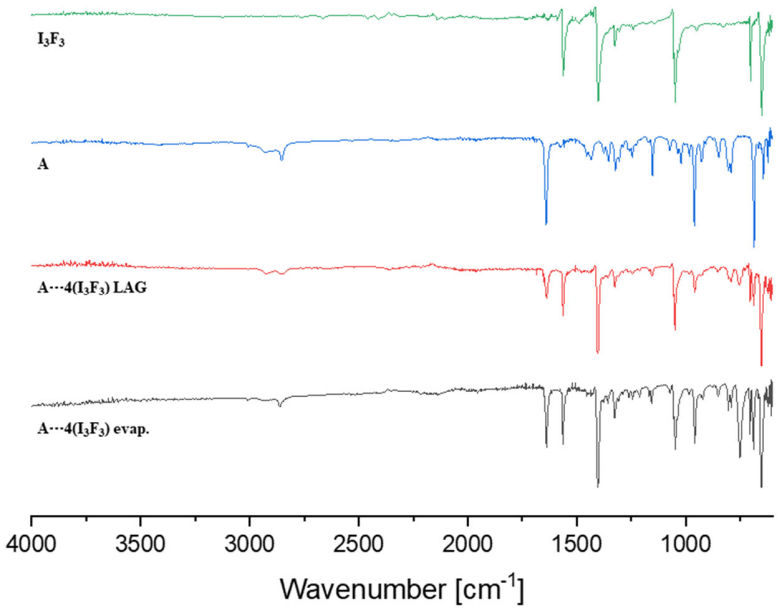

Figure S26: Measured IR-spectra of **I_3F_3** (green), acceptor **A** (blue), **A···4(I_3F_3)** synthesized by liquid assisted grinding (red) and **A···4(I_3F_3)** obtained by slow evaporation (grey).

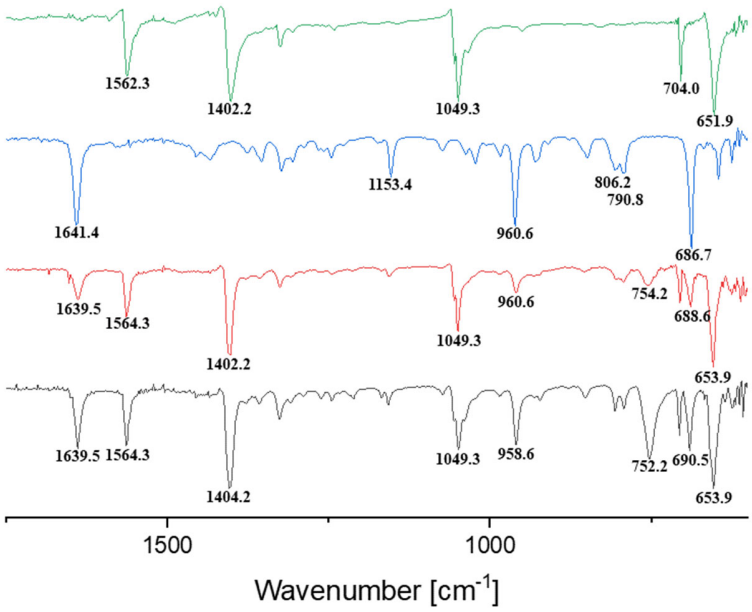

Figure S27: Enlarged detail of the measured IR-spectra of **I_3F_3** (green), acceptor **A** (blue), **A···I_3F_3** synthesized by liquid assisted grinding (red) and **A···I_2F_4** obtained by slow evaporation (grey).

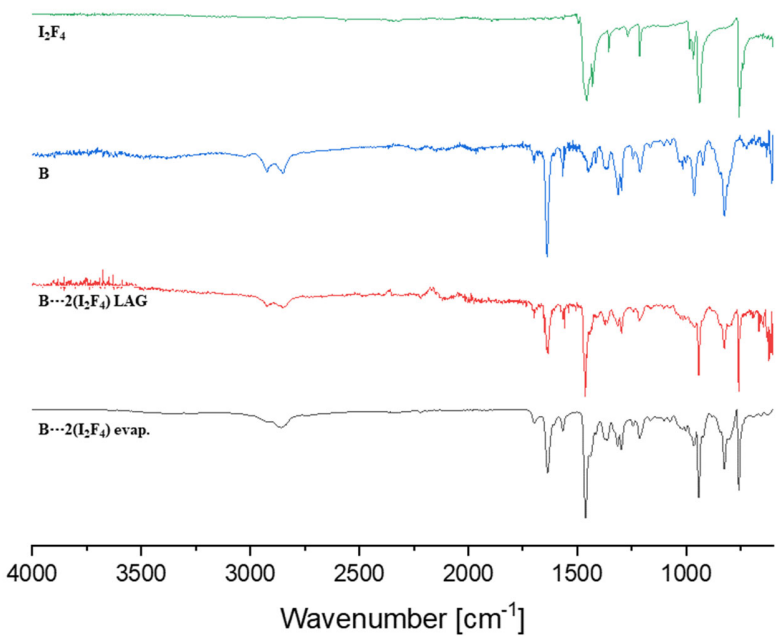

Figure S28: Measured IR-spectra of I_2F_4 (green), acceptor **B** (blue), **B**···**2**(I_2F_4) synthesized by liquid assisted grinding (red) and **B**···**2**(I_2F_4) obtained by slow evaporation (grey).

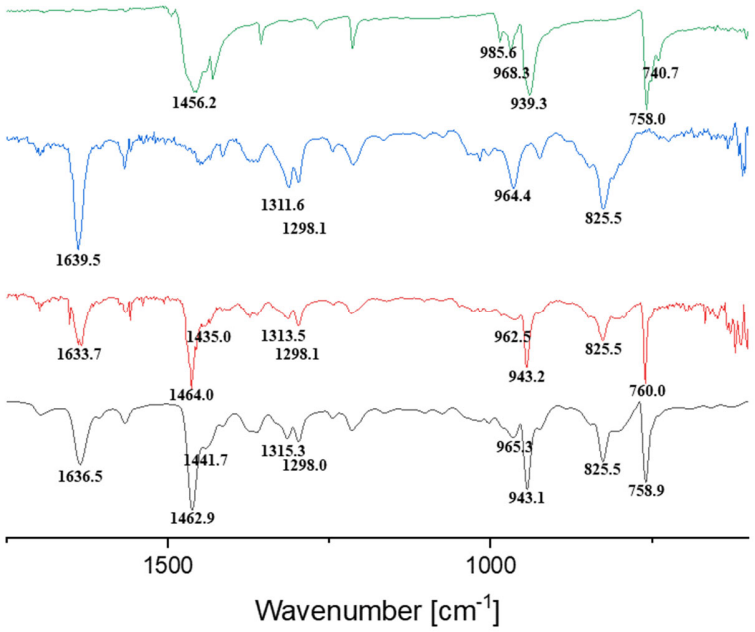

Figure S29: Enlarged detail of the measured IR-spectra of I_2F_4 (green), acceptor **B** (blue), **B**···**2**(I_2F_4) synthesized by liquid assisted grinding (red) and **B**···**2**(I_2F_4) obtained by slow evaporation (grey).

VIII. TGA

Thermogravimetric analysis was carried out under synthetic air using a Netzsch TG 209 F3 Tarsus in a temperature range from 30 °C to 600 °C at a step rate of 5 °C/min. Samples of **A···2(I_2F_4)**, **A···4(I_3F_3)**, **B···2(I_2F_4)** were obtained by slow evaporation. A sample of **B···2(I_2F_4)** was also obtained by liquid assisted grinding. Onset decomposition temperatures were derived from thermogravimetric analysis curves by tangent evaluation.

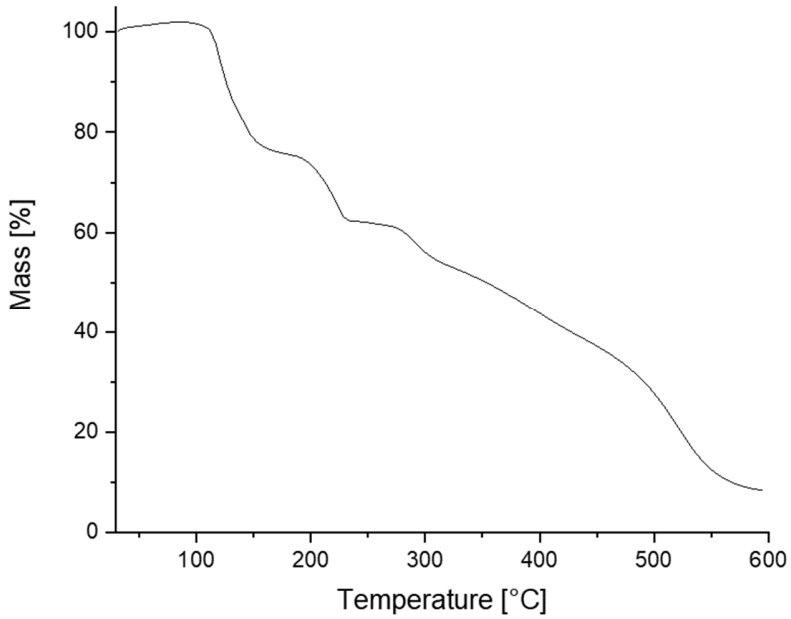

Figure S30: Measured TGA spectrum of **A···2(I_2F_4)** obtained by slow evaporation. The determined onset temperature is 111.65 °C.

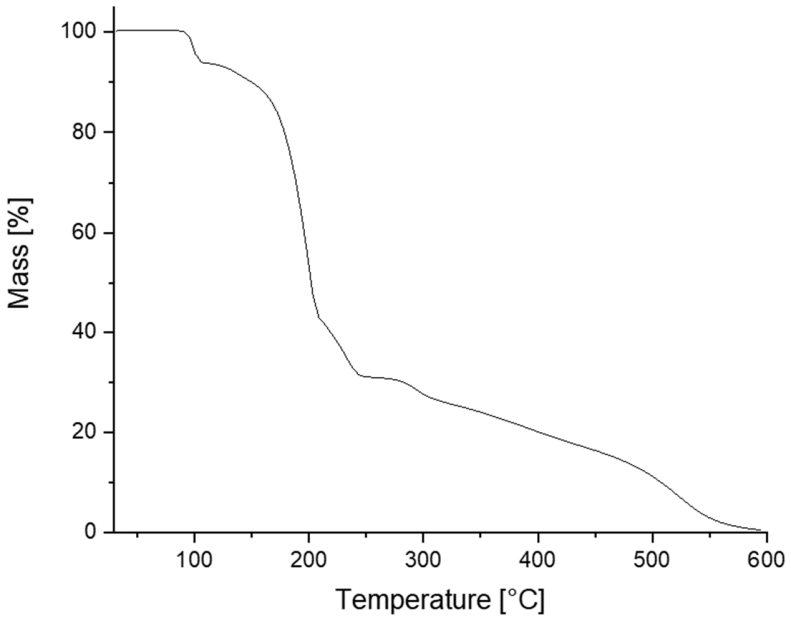

Figure S31: Measured TGA spectrum of **A···4(I_3F_3)** obtained by slow evaporation. The determined onset temperature is 91.33 °C.

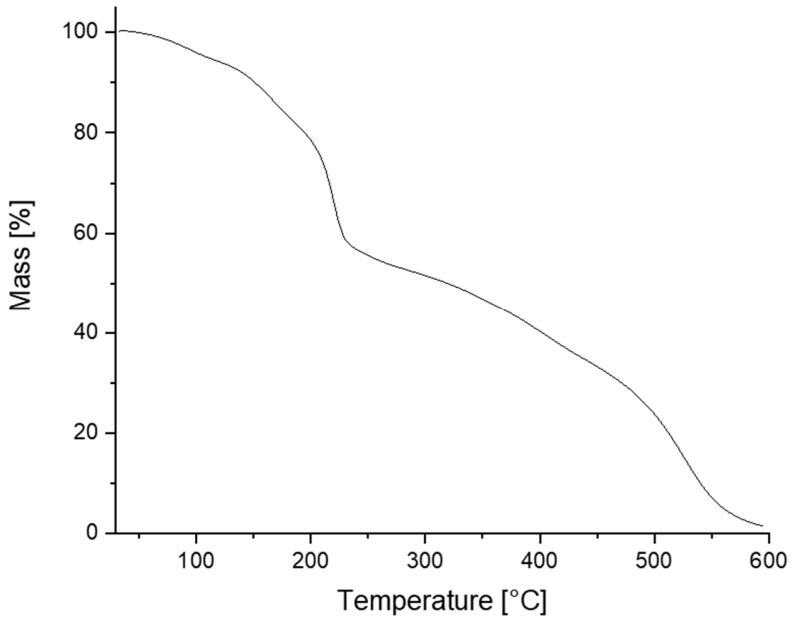

Figure S32: Measured TGA spectrum of **B···2(I_2F_4)** obtained by slow evaporation. The determined onset temperature is 108.67 °C. The initial dip is due to the evaporation of remaining solvent.

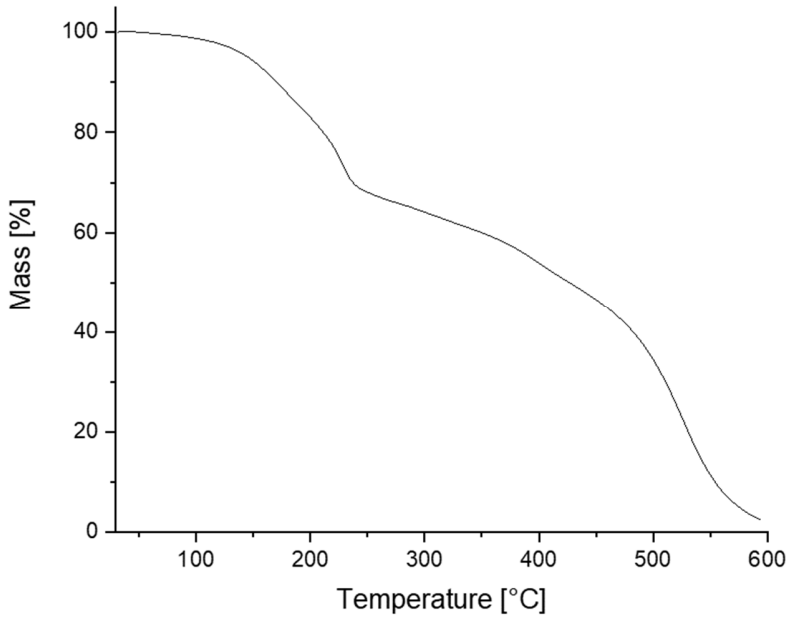

Figure S33: Measured TGA spectrum of **B···2(I_2F_4)** obtained by liquid assisted grinding. The determined onset temperature is 128.28 °C. The initial dip is due to the evaporation of remaining solvent.

As the processes of solvent loss and decomposition are overlapping at some temperatures, the determination of the onset decomposition temperatures for the samples of **B···2(I_2F_4)** is impeded, resulting in differing onset decomposition temperatures. Additionally, the amount of residual solvent in the **B···2(I_2F_4)** sample obtained by slow evaporation is significantly higher.

IX. Stability tests

Slow evaporation samples of **A···2(I_2F_4)**, **A···4(I_3F_3)**, and **B···2(I_2F_4)**, as well as **B···2(I_2F_4)** produced by liquid assisted grinding, were soaked in n-pentane. The solvent was carefully removed twice a day, and new solvent was added. After three days the solvent was allowed to slowly evaporate. For 10-16 hours, the solids were kept under high vacuum at 60 °C. Before and after heating, PXRD or IR spectra were measured. The spectra were standardized for better comparability.

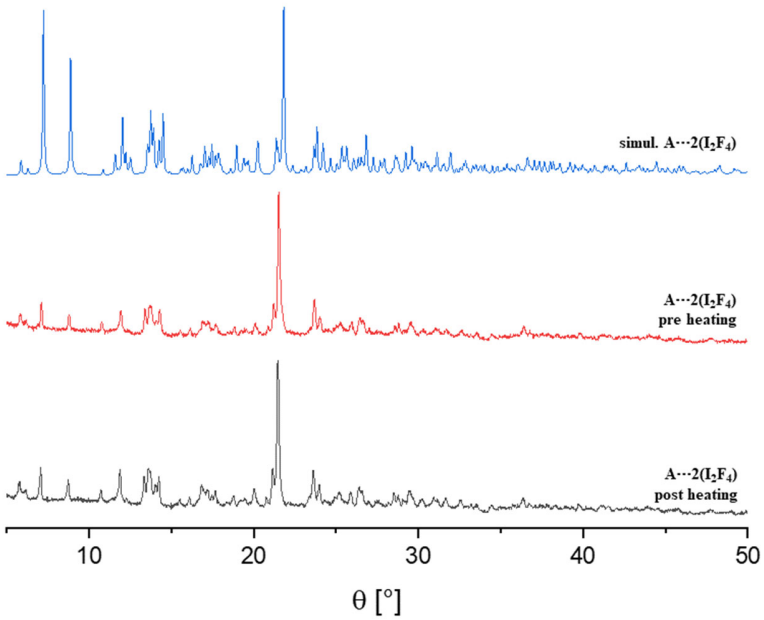

Figure S34: Simulated diffractogram of **A···2(I_2F_4)** (blue) obtained by using the SXRD data, measured PXRD spectra of **A···2(I_2F_4)** before (red) and after heating (black).

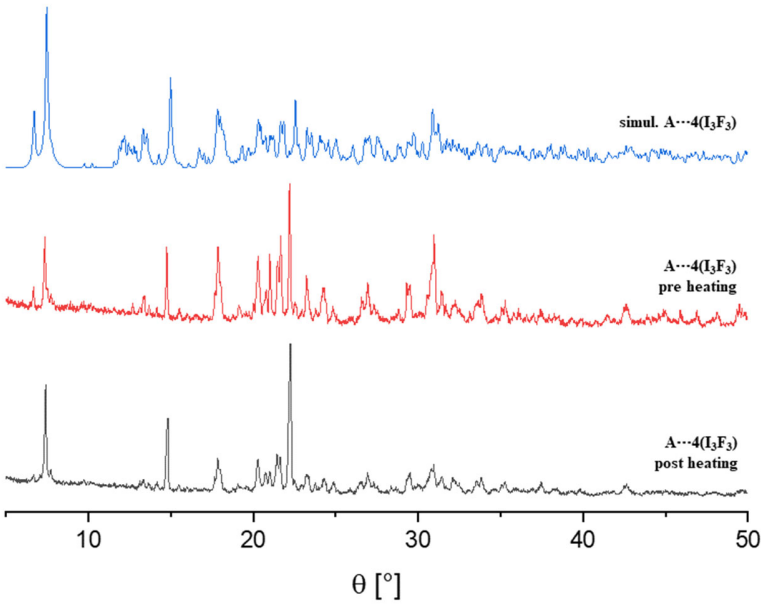

Figure S35: Simulated diffractogram of **A···4(I_3F_3)** (blue) obtained by using the SXRD data, measured PXRD spectra of **A···4(I_3F_3)** before (red) and after heating (black).

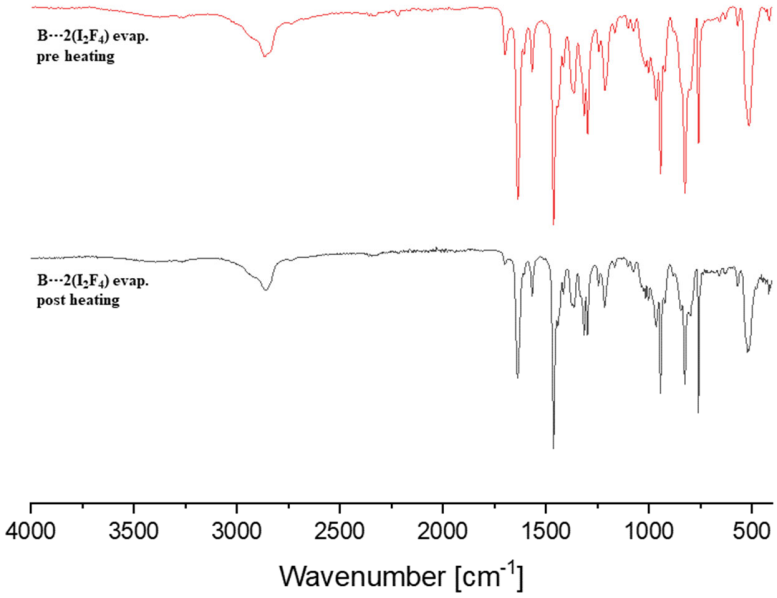

Figure S36: Measured IR-spectra of **B···2(I_2F_4)** synthesized by slow evaporation before (red) and after heating (black).

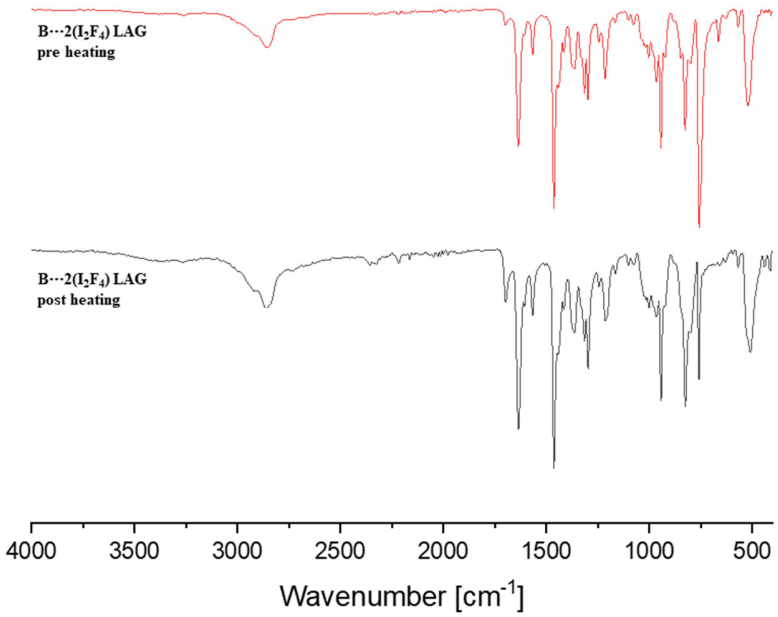

Figure S37: Measured IR-spectra of **B···2(I_2F_4)** synthesized by liquid assisted grinding before (red) and after heating (black).

X. Gas adsorption measurements

Sample preparation:

Samples of **B···2(I_2F_4)** obtained by slow evaporation and liquid assisted grinding were soaked in *n*-pentane for three days, the solvent was exchanged twice a day. After this time the solvent was allowed to evaporate in a fume hood and the sample was dried at 60 °C under high vacuum afterwards for 16 hours.

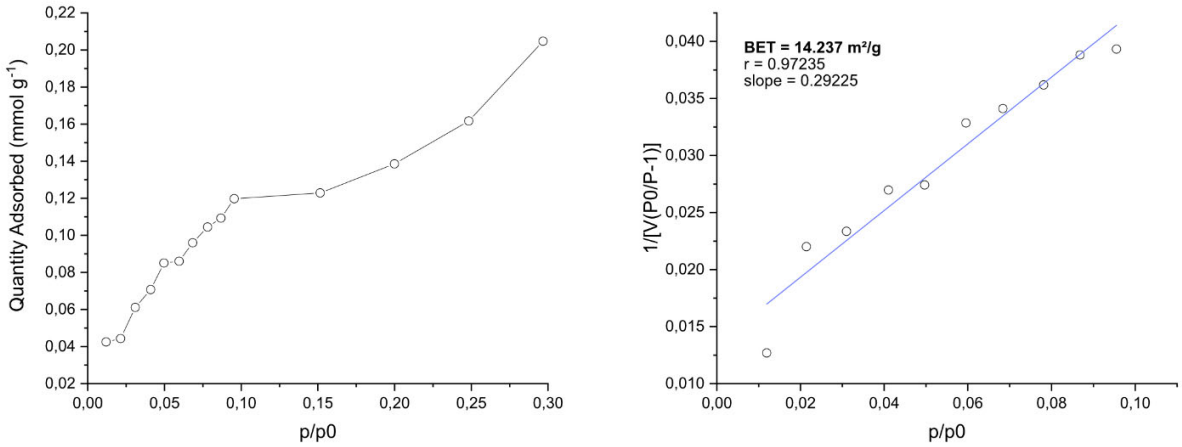

Figure S38: Left: Adsorption of nitrogen at 77 K of **B···2(I_2F_4)** obtained by slow evaporation. Right: BET plot of a sample of **B···2(I_2F_4)** obtained by slow evaporation. The BET surface area was calculated using a microporous assumption.

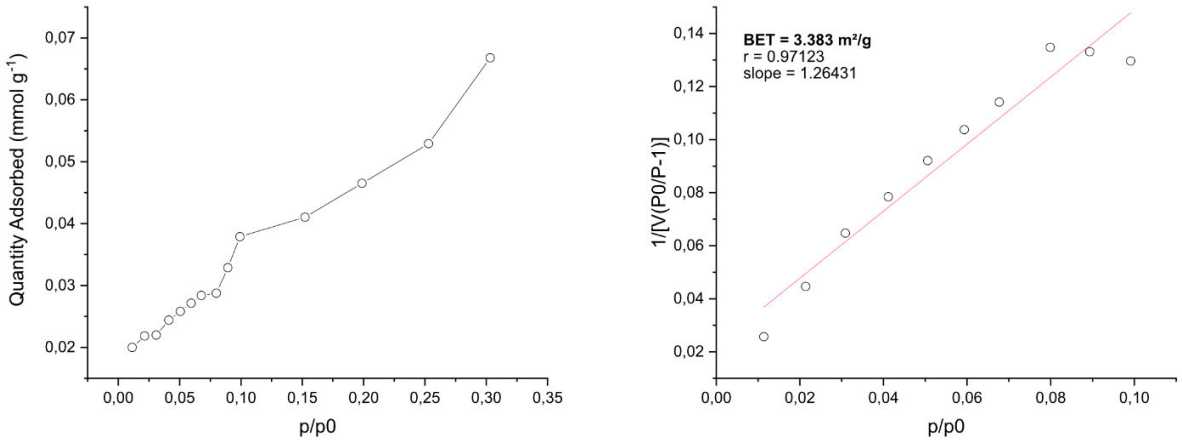

Figure S39: Left: Adsorption of nitrogen at 77 K of **B···2(I_2F_4)** obtained by liquid assisted grinding. Right: BET plot of a sample of **B···2(I_2F_4)** obtained by liquid assisted grinding. The BET surface area was calculated using a microporous assumption.

XI. References

[S1] L. C. H. Maddock, T. Nixon, A. R. Kennedy, M. R. Probert, W. Clegg, E. Hevia, *Angew. Chem. Int. Ed.* **2017**, *130*, 193-197.

[S2] M. Servalli, N. Trapp, D. Schlüter, *Chem. Eur. J.* **2018**, *24*, 15003-15012.

[S3] R. L. Greenaway, V. Santolini, M. J. Bennison, B. M. Alston, C. J. Pugh, M. A. Little, M. Miklitz, E. G. B. Eden-Rump, R. Clowes, A. Shakil, H. J. Cuthbertson, H. Armstrong, M. E. Briggs, K. E. Jelfs, A. I. Cooper, *Nat. Commun.* **2018**, *9*, 2849.

[S4] K. Hirose, Quantitative Analysis of Binding Properties in *Analytical Methods in Supramolecular Chemistry* (Ed.: C. A. Schalley), Wiley-VCH, Weinheim **2012**, 27-66.

[S5] G. M. Sheldrick, SHELXL-2014, Program for Crystal Structure Refinement, University of Göttingen, Göttingen, **2014**.

[S6] A. L. Spek, *Acta Cryst.* **2015**, *C71*, 9-18.

[S7] A. L. Spek, *J. Appl. Cryst*. **2003**, *36*, 7-11.

[S8] a) S. Muniappan, S. Lipstman, I. Goldberg*, Chem. Commun.* **2008**, *15*, 1777-1779; b) P. Smart, G. Mínguez Espallargas, L. Brammer, *CrystEngComm*, **2008**, *10*, 1335-1344; c) R. K. R. Jetti, A. Nangia, F. Xue, T. C. W. Mak, *Chem. Commun.* **2001**, *10*, 919-920.

[S9] A. Bondi, *J. Phys. Chem.* **1964**, *68*, 441-451.

[S10] R. S. Rowland, R. Taylor, *J. Phys. Chem.* **1996**, *100*, 7384-7391.

[S11] P. Giannozzi, S. Baroni, N. Bonini, M. Calandra, R. Car, C. Cavazzoni, D. Ceresoli, G. L. Chiarotti, M. Cococcioni, I. Dabo, A. Dal Corso, S. de Gironcoli, S. Fabris, G. Fratesi, R. Gebauer, U. Gerstmann, C. Gougoussis, A. Kokalj, M. Lazzeri, L. Martin-Samos, N. Marzari, F. Mauri, R. Mazzarello, S. Paolini, A. Pasquarello, L. Paulatto, C. Sbraccia, S. Scandolo, G. Sclauzero, A. P. Seitsonen, A. Smogunov, P. Umari, R. M. Wentzcovitch, QUANTUM ESPRESSO: A Modular and Open-Source Software Project for Quantum Simulations of Materials, *J. Phys.: Condens. Matter* **2009**, *21*, 395502, 1-19.

[S12] M. J. Frisch, G. W. Trucks, H. B. Schlegel, G. E. Scuseria, M. A. Robb, J. R. Cheeseman, G. Scalmani, V. Barone, G. A. Petersson, H. Nakatsuji, X. Li, M. Caricato, A. V. Marenich, J. Bloino, B. G. Janesko, R. Gomperts, B. Mennucci, H. P. Hratchian, J. V. Ortiz, A. F. Izmaylov, J. L. Sonnenberg, D. Williams-Young, F. Ding, F. Lipparini, F. Egidi, J. Goings, B. Peng, A. Petrone, T. Henderson, D. Ranasinghe, V. G. Zakrzewski, J. Gao, N. Rega, G. Zheng, W. Liang, M. Hada, M. Ehara, K. Toyota, R. Fukuda, J. Hasegawa, M. Ishida, T. Nakajima, Y. Honda, O. Kitao, H. Nakai, T. Vreven, K. Throssell, J. A., Jr. Montgomery, J. E. Peralta, F. Ogliaro, M. J. Bearpark, J. J. Heyd, E. N. Brothers, K. N. Kudin, V. N. Staroverov, T. A. Keith, R. Kobayashi, J. Normand, K. Raghavachari, A. P. Rendell, J. C. Burant, S. S. Iyengar, J. Tomasi, M. Cossi, J. M. Millam, M. Klene, C. Adamo, R. Cammi, J. W. Ochterski, R. L. Martin, K. Morokuma, O. Farkas, J. B. Foresman, D. J. Fox, Gaussian 16, Revision C.01, Gaussian, Inc., Wallingford CT, **2016**.

[S13] S. Grimme, Semiempirical GGA-Type Density Functional Constructed with a Long-Range Dispersion Correction. *J. Comput. Chem.* **2006**, *27*, 1787–1799.

[S14] T. D. Kühne, M. Iannuzzi, M. Del Ben, V. V. Rybkin, P. Seewald, F. Stein, T. Laino, R. Z. Khaliullin, O. Schütt, F. Schiffmann, D. Golze, J. Wilhelm, S. Chulkov, M. H. Bani-Hashemian, V. Weber, U. Borštnik, M. Taillefumier, A. S. Jakobovits, A. Lazzaro, *et al.* CP2K: An electronic structure and molecular dynamics software package - Quickstep: Efficient and accurate electronic structure calculations. *J. Chem. Phys.* **2020**, *152*, 194103.

[S15] Y. Zhao, D.G. Truhlar, *Theor. Chem. Acc.* **2008**, *120*, 215–241.

[S16] T. Lu, F. Chen, Multiwfn: A multifunctional wavefunction analyzer. *J. Comput. Chem.* **2012**, *33*, 580-592.
[S17] E. Espinosa, E. Molins, C. Lecomte, *Chem. Phys. Lett.* **1998**, *285*, 170.
[S18] I. Mata, I. Alkorta, E. Espinosa, E. Molins, *Chem. Phys. Lett.* **2011**, *507*, 185.
[S19] E. V. Bartashevich, V. G. Tsirelson, *Russ. Chem. Rev.* **2014**, *83*, 1181.